Single degree of freedom vortex induced vibration of undulatory seal whiskers at low Reynolds number and various angles of attack: A computational fluid dynamics study 🕫 🚳

Cite as: Phys. Fluids 36, 091920 (2024); doi: 10.1063/5.0227544 Submitted: 9 July 2024 · Accepted: 27 August 2024 ·

Published Online: 25 September 2024







Biao Geng, (D) Xudong Zheng, (D) and Qian Xue^{a)} (D)



AFFILIATIONS

Department of Mechanical Engineering, Rochester Institute of Technology, Rochester, New York 14623, USA

a) Author to whom correspondence should be addressed: qxxeme@rit.edu

ABSTRACT

The cross-flow vortex-induced vibration (VIV) response of an elastically mounted idealized undulatory seal whisker (USW) shape is investigated in a wide range of reduced velocity at angles of attack (AOAs) from 0° to 90° and a low Reynolds number of 300. The mass ratio is set to 1.0 to represent the real seal whisker. Dynamic mode decomposition is used to investigate the vortex shedding mode in various cases. In agreement with past studies, the VIV response of the USW is highly AOA-dependent because of the change in the underlying vortex dynamics. At zero AOA, the undulatory shape leads to a hairpin vortex mode that results in extremely low lift force oscillation with a lowered frequency. The frequency remains unaffected by VIV throughout the tested range of reduced velocity. As the AOA deviates from zero, alternating shedding of spanwise vortices becomes dominant. A mixed vortex shedding mode is observed at AOA = 15° in the transition. As the AOA deviated from zero, the VIV amplitude increases rapidly by two orders, reaching the maximum of about 3 times diameter at 90°. An infinite lock-in branch is present for AOA from 60° to 90°, where the VIV amplitude remains high regardless of the increase in reduced velocity.

Published under an exclusive license by AIP Publishing. https://doi.org/10.1063/5.0227544

INTRODUCTION

Whiskers, also known as vibrissae, are tactile sensory hairs emanating from follicles. They are found in most terrestrial and aquatic mammals (Grant and Goss, 2022). Since there are no nerves inside the hair shaft, sensing is realized through the sensory receptors in the highly innervated follicle-sinus complex (F-SC) that sense pressure and distortion when the whiskers are bent by external loading (Sofroniew and Svoboda, 2015). The follicle-sinus complexes of the pinnipeds (commonly known as seals) are the most developed among all mammals (Marshall et al., 2006). Compared to terrestrial mammals like rats and beavers with only 100-120 nerves per whisker, pinnipeds like ringed seals have astonishingly an order of magnitude more innervation (Hyvärinen and Katajisto, 1984). This remarkable difference in innervation signifies the importance of the pinniped whiskers as a sensing organ (Dehnhardt et al., 1999). Indeed, it translates to the exquisite tactile sensitivity in pinniped whiskers. For example, Dehnhardt et al.. (1998) showed that a harbor seal (stationary) can detect dipole water movement as low as 245 µm/s using its whiskers.

Murphy et al. (2015) reported a harbor seal responding to tactile stimuli to their whiskers as low as 0.09 mm/s at 80 Hz. Such sensitivity was shown to be comparable to the touch of the human hand. Evidence also showed that a California sea lion had comparable or even higher tactile sensitivity than the harbor seals (Dehnhardt et al., 2008).

The hair shaft of the whiskers transfers external loading to the sensory system. They are generally slender, tapered, and curved keratinous structures that are arranged in groups most commonly around the muzzle. Unlike terrestrial mammals whose whiskers are round in cross section, the whiskers of the pinnipeds are flattened. This differentiation of pinniped whiskers is likely the result of adaptation to their aquatic lifestyle which requires sensing of the hydrodynamic environment. There are two major types of whisker morphology among the pinnipeds (Dehnhardt et al., 2008; Ginter et al., 2012; Hanke et al., 2010; and Murphy et al., 2013). The smooth seal whisker (SSW) represented by those of the California sea lion features a smooth surface structure and has a slightly flattened oval cross section (aspect ratio 1:1.25). The undulatory seal whisker (USW) represented by those of the harbor seal features an undulated surface structure and is more flattened in the cross section (aspect ratio 1:2–1:4) (Miersch et al., 2011). While both harbor seals and California sea lions were found to be capable of following hydrodynamic trails effectively using their whiskers, experiments showed that the harbor seals can detect older and weaker hydrodynamic trails than the California sea lion (Dehnhardt et al., 2001; Gläser et al., 2011). The elevated sensitivity of harbor seal whiskers is commonly attributed to the undulation feature, which has been the focus of the research on flow past seal whiskers and many seal whisker inspired sensor designs.

Hanke et al. (2010) parameterized the USW morphology using a seven-parameter model [Fig. 1(a)], which has since been widely adopted in seal whisker models. Neglecting the tapering and curvature of the whisker, the shape of USWs is roughly a slender cylinder featuring an elliptical cross section and undulation along the shaft. The undulation of the major axis (chord length) and minor axis (thickness) of the elliptical cross section has a 180° phase difference. The cross sections are not perpendicular to the whisker shaft. Instead, they have various offset angles with respect to the longitudinal hair shaft axis, which is referred to as the offset angle or angle of incidence (Rinehart et al., 2017).

The specialized shape of USWs has been shown to suppress hydrodynamic force oscillation, and consequently vortex induced vibration (VIV), by breaking the coherence of the Kármán vortices when the narrow side faces the flow. The lift force oscillation is more than one order of magnitude smaller compared to elliptical cylinders (Hanke *et al.*, 2010; Kim and Yoon, 2017; and Liu *et al.*, 2019b). By eliminating the offset angles in the whisker and using periodic boundary conditions in their simulations, Liu *et al.* (2019b) observed highly

organized streamwise wake structures with interlocked vortex tubes shaped like a hairpin, hence the term "hairpin vortex" [Fig. 1(b)]. Such wake structure was caused by the 180° phase difference in the undulation of the chord length and the thickness and was found to exist in wide ranges of shape parameters and Re. The suppression of lift oscillation by the undulation is hypothesized to reduce the self-induced noise in the sensory system for the seals during forward swimming, making the USWs more sensitive to wakes left behind by other swimming objects (Hanke et al., 2010; Miersch et al., 2011). However, this understanding of the role of the undulation in the USWs is based on the zero angle of attack (AOA) orientation only with a few flow speeds. The hydrodynamic conditions real seal whiskers are subjected to can be much more complex.

The effect of AOA is important since a wide range of AOAs could occur as the animal navigates through the water. First, seals have an array of whiskers with a wide distribution of orientation (Graff, 2016). While the pinnipeds lack the musculature for individual whisker control like the rat or the mouse, they can protract their array of whiskers through the mystacial pad (Miersch et al., 2011; Sofroniew and Svoboda, 2015). Second, navigation underwater involves both forward swimming and turning. The AOA of the whisker can also be affected by the head movement, which is typical as the animal actively searches for trails (Dehnhardt et al., 2001; Gläser et al., 2011). Finally, the hydrodynamic environment could have complex flows that pose a large range of AOAs to the whiskers.

Another parameter of importance is the reduced velocity, which measures the flow speed in relation to the natural frequency and diameter of the whiskers. Since the whiskers in the array varies greatly in length, their natural frequency also varies greatly [see a summary in

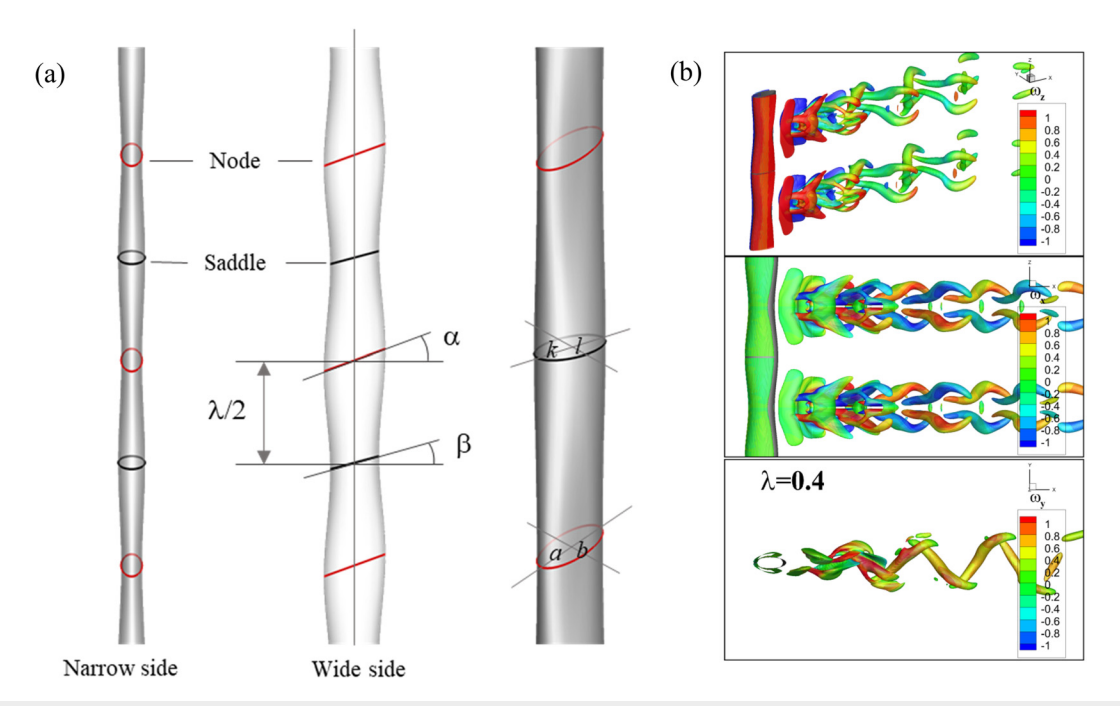


FIG. 1. (a) The undulation feature of the undulatory seal whiskers, following the seven-parameter model by Hanke *et al.*(2010). The parameters are as follows: the semi-major and semi-minor axis length at the node (a and b) and saddle (k and l) planes; the offset angles at the two planes (α and β); and the undulation wavelength (λ). (b) Highly organized hairpin vortex generated by USWs at zero AOA.

Zheng *et al.* (2021)], leading to a wide range of reduced velocity even at the same swimming speed. The number of studies investigating the effect of these two parameters is limited.

Kim and Yoon (2017) used large eddy simulation to study the effect of AOA on flow characteristics around a stationary USW at the Reynolds number of 500. They showed that for small AOAs (<15°), the lift force oscillation of the USW was almost negligible. When AOA increased beyond 15°, the amplitude of the lift force oscillation increased, reached a plateau around 50°, and then remained almost constant up to 90°. The authors concluded that as AOA increases, the bluff body flow overcomes the flow induced by the USW shape, resulting in almost the same flow and magnitude of forces as the elliptic cylinder.

Murphy et al. (2013) tested VIV responses of real seal whiskers oriented at 0°, 45°, and 90° against an incoming flow of 0.5 m/s. The whiskers were mounted as cantilever beams. Vibration velocity was up to 60 times higher when AOA was 90° compared to 0°. A particular interesting finding in this study was that the SSWs of the California sea lion showed close VIV response amplitude to that of the USWs under the tested AOAs, raising questions on the role of the undulation in seal whisker sensing.

Beem (2015) studied the VIV responses of scaled up whisker models (mass ratio from 0.5 to 1.1) using a forced vibration setup, in which the responses can be regarded as representative of free vibration if the energy transfer is from the flow to the whisker model. The amplitude and frequency of the forced vibration and the AOA were parametrically varied, and the wake structures were studied using PIV. It was found that VIV reduction diminished when flow approached the whisker from larger AOAs. Beyond 45°, the whisker responded similarly to a smooth elliptical cylinder with similar wake structures consisting of strong coherent vortices. One limitation of this study was that the vibration frequency and reduced velocity were not varied independently.

Wang and Liu (2017) investigated the effect of AOA and reduced velocity on the VIV response of the USW using a scaled-up model at a Reynolds number of 1800. The in-air experimental results showed that the USW began to have appreciable oscillation amplitude at 45° AOA. The maximum oscillation amplitude increased with AOA from about 0.06D (measure of whisker diameter) at 45° to 0.35D at 90°. The reduced velocity for significant oscillation was between 5 and 8. The VIV amplitude of the USW was in contrast with the 0.03D of a circular counterpart. Due to the experiment being conducted in air, the mass ratio was 500, which was significantly higher than that of a seal whisker.

Similar model experiments have also been conducted in water (Song et al., 2022; Wei et al., 2023) with a much lower mass ratio of 10. The USW model started to show significant VIV when AOA reached 30° and reached a peak amplitude as high as 3D at 90°. In these two studies, the performance of the USW model was compared to that of an equivalent elliptical cylinder, which showed similar VIV response across the AOA and reduced velocity, except for a narrow lock-in region at small, reduced velocity and zero AOA.

Despite previous research on the VIV of USWs, there lacks a systematic investigation of this problem at the mass ratio of 1.0, which is the realistic value since the seal whisker density is close to water density (Kamat *et al.*, 2023; Shatz and de Groot, 2013). Mass ratio is a key parameter affecting the nature of VIV of a system (see Williamson and

Govardhan, 2004, for a review). Two distinct types of VIV response exist for the circular cylinder depending on the mass ratio. For high mass ratio systems, the amplitude response curve has two branches: an initial branch and a lower branch; whereas for low mass ratio systems, there exists an additional higher branch with elevated amplitude. The range of reduced velocity for synchronization between vortex shedding and structure oscillation also increases as the mass ratio becomes lower. Furthermore, when the mass ratio is lower than a critical mass ratio, the range of reduced velocity of resonant oscillation extends to infinite, which is termed the infinite lock-in regime/branch. For circular cylinders, the critical mass ratio was found to be 0.54 (Govardhan and Williamson, 2002). This value is shape dependent. Previously, infinite lock-in was observed for an elliptical cylinder with a mass ratio of 1.0 (Leontini et al., 2018).

This study aims to quantify the single DOF VIV response of undulatory seal whiskers with a mass ratio of 1.0 under low Reynolds number. This is an effort toward providing normative data for seal-whisker inspired sensor designs. By systematically comparing the VIV characteristics of circular cylinders, elliptic cylinders, and USWs, a better understanding of the role of the undulation and the sensing mechanisms in pinnipeds could be derived.

SIMULATION SETUP

The flow field was simulated using an in-house incompressible Navier–Stokes solver, which employs a sharp-interfaced immersed-boundary-method to accurately resolve the immersed structure. The vibration of the whisker was computed using the average acceleration Newark scheme. The interaction between the flow and whisker vibration was modeled using an implicit coupling scheme. The implementation of this solver setup has been validated previously (Liu *et al.*, 2019a) for canonical flow–structure interaction (FSI) problems with solid/fluid density ratios of 1 and 10. For brevity, details of the numerical algorithm are not included here; interested readers can find further information in Liu *et al.* (2019a).

The whisker geometry [depicted in Fig. 2(a)] was adopted from a previous study (Liu *et al.*, 2019b), which employed a further idealized version of the seven-parameter model proposed by Hanke *et al.* (2010). The rostral-caudal slant angle (the offset angle) was not considered. The exclusion is based on the observation that the offset angle displays a rough Gaussian distribution centered around zero, suggesting that the offset angle is not an optimized feature (Kamat *et al.*, 2023; Rinehart *et al.*, 2017). Specifically, the whisker is represented as a straight elliptical cylinder with undulating major and minor axis in the cross-sectional ellipse. Its shape is defined by five parameters: the semi-major axis *a* and semi-minor axis *b* at the node plane, the semi-major axis *k* and semi-minor axis *l* at the saddle plane, and the wavelength λ of the undulation. The undulation of the semi-major (*m*) and semi-minor (*n*) axes along the shaft (*z*) are given by sinusoidal functions as follows:

$$m(z) = \frac{a+k}{2} + \frac{a-k}{2} \cos\left(\frac{2\pi z}{\lambda}\right),$$

$$n(z) = \frac{b+l}{2} + \frac{b-l}{2} \cos\left(\frac{2\pi z}{\lambda}\right).$$

The mean hydraulic diameter, denoted as \overline{D} , is used as the characteristic length. It is the mean of the hydraulic diameters at the saddle and node planes. The hydraulic diameter is defined as D=4S/C, where

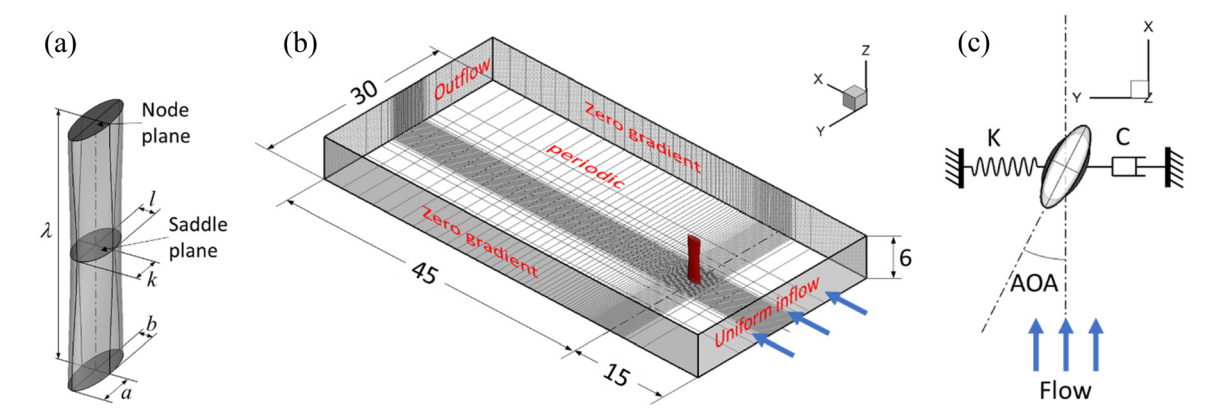


FIG. 2. Simulation setup. (a) Whisker geometry. (b) Simulation domain and boundary conditions. All dimensions are normalized by \overline{D} . The grid lines show the non-uniform distribution of the Cartesian grid (plotted at a coarser level). (c) Single degree-of-freedom whisker setup from the top view.

D, S, and C are the hydraulic diameter, area, and circumference of an ellipse, respectively. The feature dimensions were based on measurements reported in Rinehart *et al.* (2017) and is listed in Table I. The aspect ratio of the elliptical cross section (chord/thickness) varies from 2.95 at the node plane to 1.89 at the saddle plane. Like the seven-parameter model adopted in many previous studies, the model did not include tapering.

The simulation domain is represented by a $60 \times 30 \times 6\overline{D}$ rectangular box [Fig. 2(b)]. The domain is discretized using a Cartesian mesh. 256 non-uniform grid intervals were used along the X and Y directions with a $3 \times 5\overline{D}$ region enclosing the whisker, where a uniform high resolution of $0.025\overline{D}$ was used to resolve the whisker geometry. A uniform grid was used in the Z direction with a resolution of 0.09385λ . The details of the employed grid and a grid independence study can be found in the Appendix.

The whisker geometry was discretized using a structural triangular mesh with 52 intervals along the circumference and 50 intervals along one wavelength. Due to the slender structure of real whiskers, it is computationally too expensive to include the whole hair shaft while resolving the undulation feature. Instead, segments of a few wavelengths with periodic boundary conditions have been used in previous simulations (Dunt *et al.*, 2024; Kim and Yoon, 2017; Liu *et al.*, 2019b; and Witte *et al.*, 2012). Kim and Yoon (2017) compared simulation results using segments of 2, 3, and 4 wavelengths for 0° and 90° angles of attack. They found that both the mean amplitude and the frequency of lift force oscillation were captured accurately by the two-wavelength cases under both AOAs. Moreover, the wake structure showed repeated one-wavelength patterns along the whisker. Similar periodic flow features were more recently reported by Dunt *et al.* under 0°

TABLE I. Simulation parameters (length normalized by \overline{D} =0.533 mm).

FSI parameter	Re 300	m* 1	$m^*\xi$ 0.02	<i>U</i> _r 2–15 (50)	AOA 0°∼90°
Whisker parameter	λ 6	а 0.985	<i>b</i> 0.334	<i>k</i> 0.778	<i>l</i> 0.411

AOA for wavelengths between 5 and 6.86. This range covers the wavelength of 6 used in the current study. These previous results show that the main periodic flow feature of the USW is recurring at one wavelength. Therefore, a good representation of the flow features and VIV characteristics can be expected from simulations using a one-wavelength segment. Changing from two wavelengths to one wavelength also substantially reduces the computational cost. With these considerations, a segment of one wavelength of the idealized whisker is placed along Z direction, along which the periodic boundary condition is applied at the top and bottom of the domain. For velocity, a constant inflow velocity is applied to the upstream boundary. The downstream boundary is free outflow. Zero-gradient condition is applied to the lateral boundaries. Zero-gradient condition is employed for the pressure at all the boundaries. All boundary conditions are homogeneous.

The whisker is modeled as a single DOF rigid body connected with a spring and a damper [Fig. 2(c)]. AOA is defined as the angle between the uniform incoming flow and the major axis of the whisker cross section.

In this study, the density ratio, m^* , is set to 1.0 due to the close proximity of the density of seal whiskers and water. The damping ratio, ξ , is chosen as 0.02 to match the structural damping of seal whiskers (Hans *et al.*, 2014). To explore the influence of the reduced velocity, $U_{\rm r}$, defined as $U_{\rm r} = \frac{U_{\infty}}{f_{\rm rw}D}$, we adjusted the stiffness of the spring (and thus, the *in vacuo* natural frequency $f_{\rm nv}$) while maintaining a fixed incoming flow speed of $U_{\infty} = 0.57\,{\rm m/s}$. Based on the typical seal's swimming speed and range of natural frequencies of seal whiskers, $U_{\rm r}$ was varied from 2 to 15 with an increment of 1. The AOA is varied from 0° to 90° with an increment of 15°. Each case in the parametric space is defined by the AOA and $U_{\rm r}$. To test the existence of the infinite lock-in branch, larger $U_{\rm r}$ (up to 50) was simulated for AOA from 60° to 90°. The simulation setup parameters are summarized in Table I.

With this setup, it is worth noting that the reduced velocity and Reynolds number are defined based on the hydraulic diameter of the whisker, and thus remains constant regardless of the AOA. However, as AOA changes, it affects the projected frontal diameter, resulting in variation in the effective reduced velocity and Reynolds number for different AOAs.

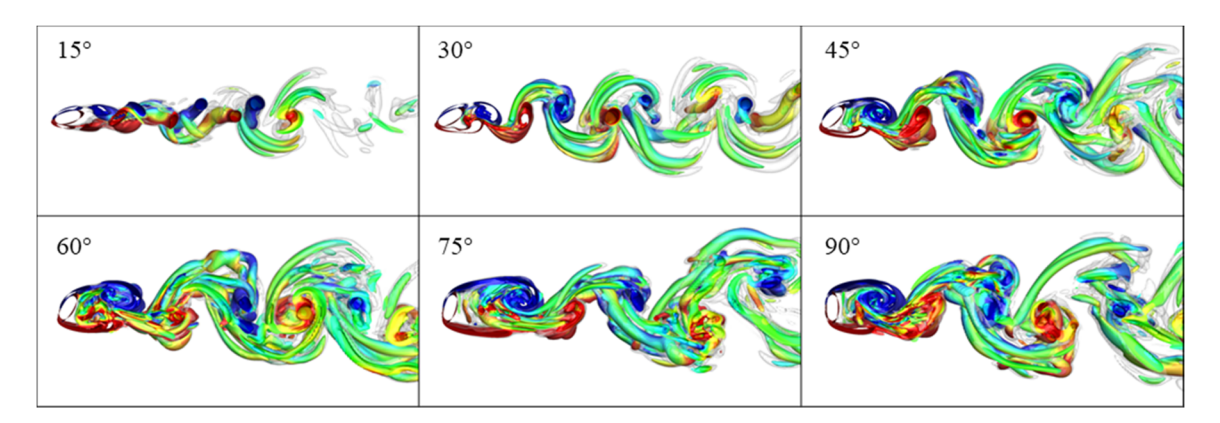


FIG. 3. Top view of the wake structures of flow past a stationary USW at non-zero AOAs.

RESULTS AND DISCUSSION Flow past stationary whiskers

To facilitate the analysis of VIV cases, flow past stationary whisker simulations were also conducted, capturing the flow characteristics at different AOAs. These simulations utilized the same setup as the VIV cases with the exception of the fixed whisker. Figure 3 illustrates wake patterns observed for non-zero AOAs. Vortex structures are visualized by the iso-surface of the imaginary part of the complex eigenvalue derived from the instantaneous velocity gradient tensor, which quantifies the local rotation of the flow (Mittal and Balachandar, 1995). The color of the iso-surfaces represents spanwise vorticity. Across all the illustrated cases, the wake structures exhibited characteristics of a typical Karman vortex street, featuring alternating blue-red pairs of spanwise vortices, which leads to lift oscillation. This contrasts with the hairpin vortex mode at zero AOA [see Fig. 1(b)].

The lift force spectra for these cases were computed as references for analyzing the VIV results. The dominant frequencies of lift force for these cases are plotted in Fig. 4(a) (triangles), revealing a nonlinear trend with AOA. Upon normalization with respect to \overline{D} , the dominant nondimensional frequency, St = $\frac{f\overline{D}}{U_{\infty}}$ starts approximately from 0.184 at AOA = 0°, then slightly increases to 0.190 at AOA = 15° where a second prominent frequency of 0.255 is also present. The corresponding spectrum for the lift force at AOA = 15° is shown in Fig. 4(c),

where a smaller third peak is also observable, representing the beat frequency (0.065) of the two higher peaks. Beyond AOA = 30°, a gradual decrease in St is observed, reaching approximately 0.1 at AOA = 90°. The frequency-AOA relation of the USW is compared to that of an equivalent elliptic cylinder with the same hydraulic diameter [Fig. 4(a) crosses]. The two trends converge for AOA beyond 30°. For smaller AOAs, especially zero AOA, the frequency of the USW is significantly lower than that of the elliptic cylinder. The comparison is consistent with previous findings using large eddy simulations at Re = 500 (Kim and Yoon, 2017), suggesting that the undulatory shape loses its effect as the AOA increases. The overall upward offset in Kim and Yoon's result could be due to a shorter undulation wavelength (λ = 2.65 \overline{D}) used in their study (Dunt *et al.*, 2024).

Since the frontal dimension facing the flow increases with AOA, it is more appropriate to consider a nondimensional frequency $\text{St}^* = \frac{f\overline{D}_f}{U_\infty}, \text{ where } \overline{D}_f \text{ denotes mean frontal diameter. It is the mean of the projected width } D_f \text{ of the elliptic cross sections at the saddle and node plane on the Y-Z plane. } D_f \text{ can be calculated as } D_f = 2\sqrt{[m\sin(AOA)]^2 + [n\cos(AOA)]^2}. \text{ The result is plotted in Fig. 4(b). For the USW, at AOA = 0°, St* is the lowest (\approx0.14), whereas at AOA \geq 60°, St* is relatively constant (\approx0.18), a value consistent with elliptical cylinders of comparable aspect ratios and$

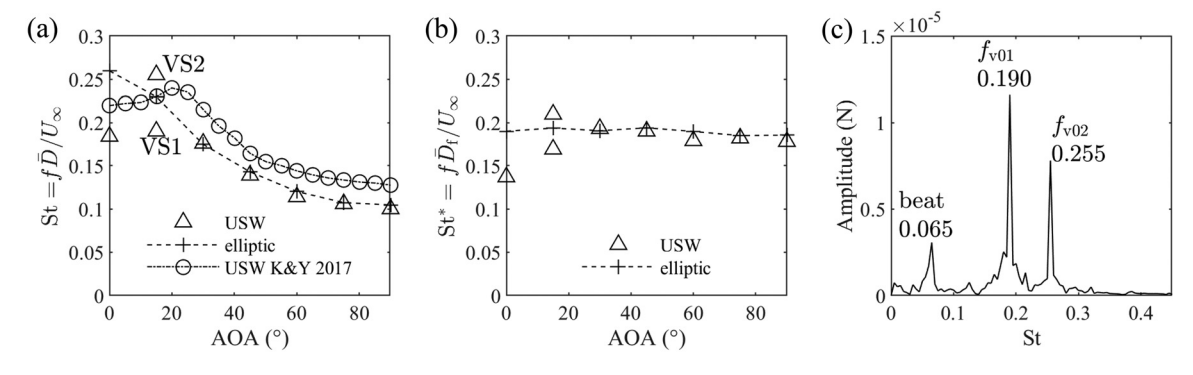


FIG. 4. Dominant lift force frequencies for flow past stationary whiskers at various AOAs, normalized based on \overline{D} (a) and mean frontal dimension \overline{D}_f (b), respectively. The dashed line with crosses is for an elliptical cylinder of the same hydraulic diameter as the whisker. USW K&Y is from Kim and Yoon (2017). The overall upward offset could be due to a shorter undulation wavelength used in their study. (c) Lift force spectrum of the AOA = 15° case.

Reynolds number (Radi et al., 2013). For the elliptic cylinder, St* remains relatively constant regardless of AOA. The change of St* with AOA is through multiple factors. First, the effect of the shape change must be considered. Second, the Re based on \overline{D}_f changes with AOA from 220 at AOA = 0° to 530 at AOA = 90° , and its effect on the Strouhal number must be considered. It has been observed in the low Re range (from Re = 200 up to Re = 1000) in experiments on elliptic cylinders that the Strouhal number increases with Re and with the stream-wise to cross-flow dimension ratio (Kurtulmuş, 2022; Radi et al., 2013). For the elliptic cylinder in Fig. 4(b), the St* at $AOA = 0^{\circ}$ (0.190) and 90° (0.186) are very close, which could be the combinatory effect of both Re and aspect ratio. This suggests that for the elliptic cylinder and for the USW at AOA ≥ 30°, the frequency decrease with AOA in Fig. 4(a) is mainly due to the increase in frontal dimension with AOA. The lower frequency of the USW at zero AOA, on the other hand, arises from the lower St*, which is related to the hairpin vortex shedding mode.

The above comparison with the elliptic cylinder shows that in addition to the suppression of lift oscillation, the hairpin vortex shedding also significantly lowers the oscillation frequency compared to vortex shedding frequency of an elliptical cylinder of similar aspect ratio (~30% reduction). The frequency lowering effect of the undulation was also observed in previous simulations and experiments of whisker-like cylinders at higher Reynolds numbers (Hans et al., 2013; Kim and Yoon, 2017). Hans et al. (2013) suggested that the lowered frequency could contribute to longer structural life. Lyons et al. (2020) showed a similar observation with DNS simulation, which was later confirmed in an experimental study (Ferčák et al., 2023).

The existence of more than one vortex shedding frequency in flow past modified cylinders have been reported in the literature in various settings (Gaster, 1969; Papangelou, 1992; and Tombazis and Bearman, 1997). For example, Tombazis and Bearman (1997) showed, for cylinders with a half-elliptic nose and a sinusoidal trailing edge, a dual frequency characteristic where two vortex shedding frequencies coexist and alternate along the span. The phenomenon was confirmed to exist robustly in a wide range of Re from 2500 to 60 000. In our AOA = 15° case, the lower vortex shedding frequency, as will be shown in a later section, corresponded to wake structures at the saddle plane, similar to where the hairpin vortices form; this is referred to as the saddle mode hereafter. The St* is higher than that of the hairpin vortex shedding. The higher prominent frequency corresponded to a mode resembling the classic Karman vortex shedding near the node plane, referred to as the node mode hereafter. The deviation of St* from the elliptic cylinder suggests that it is influenced by the saddle mode due to their coexistence and interaction. Some related discussion can be found in Tombazis and Bearman (1997).

A similar dual frequency characteristic has also been previously observed in flow past USWs at 0° AOA (Chu et al., 2021; Ferčák et al., 2023; Lyons et al., 2020; and Wang and Liu, 2016). It was shown specifically that the node mode has the higher frequency (Chu et al., 2021; Ferčák et al., 2023; Jie and Liu, 2017; and Wang and Liu, 2016). While it was not explicitly pointed out in an earlier study (Liu et al., 2019b), mixed vortex shedding modes were also present (see Fig. 13 in the reference). At 0° AOA, the emergence of the dual frequency vortex shedding appears to occur when the wavelength is too larger than the realistic value, which is confirmed through revisiting the data. This also appeared to be the case in the trend reported in Ferčák et al.

(2023). Reduction in the undulation amplitude of the minor axis could also lead to emergence of the dual frequency(Lyons *et al.*, 2020). In the current case (AOA = 15°), the emergence of the dual frequency was due to the deviation from zero AOA.

In summary, the frequency trends converge in current simulations with literature data on the vortex shedding frequency of elliptical cylinders and USWs. The current data highlight the frequency lowering effect of the USWs at low AOA and low Re. Deviation from such flow conditions or deviation from the realistic USW morphology diminishes or breaks this effect, leading to higher shedding frequencies or the emergence of dual frequencies. While the lower frequency was observed previously in several studies, its implication was not brought to attention. Given that this effect is a deviation from the circular to elliptical cylinder trend (unlike the lift oscillation suppression, which continues the improvement from circular to elliptical cylinders), it merits more research to understand whether the lower frequency plays some roles in the optimization of the undulatory whisker shape through evolution or it is just a by-product of the suppression of lift oscillation.

VIV response

VIV simulations were conducted until a stable limited-cycle vibration was achieved, usually spanning 10–20 cycles. In some cases, steady vibration was not achieved even after prolonged simulation duration. These cases were not pursued further. Representative cases are shown in Fig. 5, where the curves represent the time history of the displacement. The segments used for analysis are denoted. For the cases exhibiting steady vibration, the transient stage was carefully identified and subsequently excluded from the data analysis. For the cases without steady vibration, the initial developing stage where the amplitude was significantly different from the rest of the curve was excluded from data analysis.

Oscillation amplitude

The overall amplitude \overline{A} was calculated as the root mean square value multiplied by $\sqrt{2}$, given by $\overline{A} = \sqrt{2} \sqrt{\frac{1}{N} \sum_{i=1}^{N} \left(y_i - \overline{y} \right)^2}$, where i is the sample index, N is the total number of samples, and \overline{y} is the mean y coordinate. For a sinusoidal signal, the overall amplitude equals the amplitude of the dominant frequency component.

Figure 6(a) depicts the contour of VIV amplitude. The vertical axis represents the AOA. The horizontal axis represents the effective reduced velocity, $U_{\rm r}^*$, defined as $U_{\rm r}^* = U_{\infty}/(f_{\rm nv}\overline{D}_{\rm f})$. It is evident that the VIV amplitude increases substantially as AOA increases from 0° to 90° .

Figures 6(b) and 6(c) are the line plots of VIV amplitude for AOAs > 0° and AOA = 0°, respectively. At AOA = 0°, the amplitude curve resembles typical amplitude response of a forced system going through resonance, reaching a peak amplitude $\sim\!0.002\,\overline{D}$ at $U_r^*\sim\!5.4$. However, due to the small amplitude, the response at AOA=°0 was often imperceptible in experimental measurements conducted on scaled-up whisker models (Wang and Liu, 2017; Wei *et al.*, 2023). Murphy *et al.* (2017; 2013) reported the vibrational velocity at this AOA from experiments on cantilevered real whiskers around 0.007 m/s, the converted order of magnitude of displacement is comparable to the current simulation results.

At AOA = 15°, the VIV amplitude remains relatively small ($\sim 0.02 \, \overline{D}$) except for the $U_r^* = 2.3$ where a strong resonance occurred

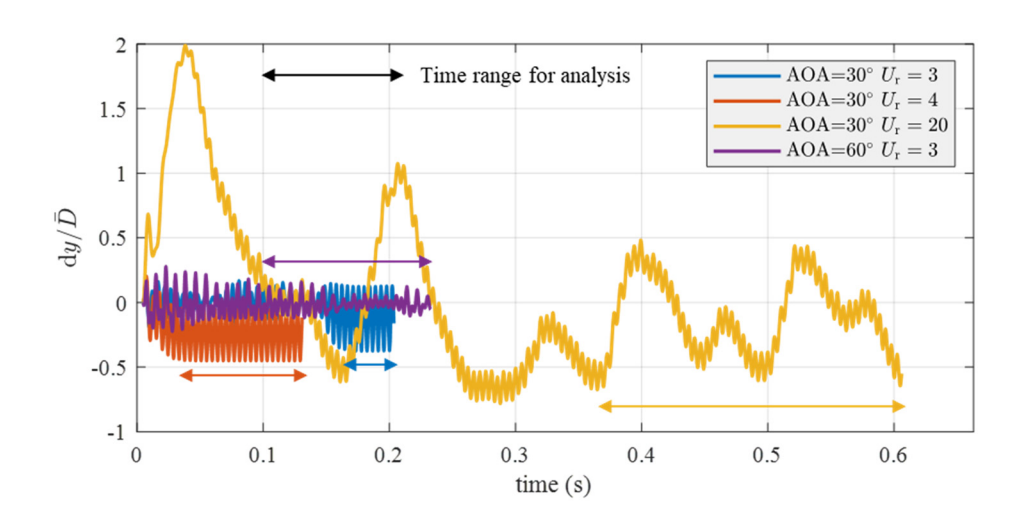


FIG. 5. Representative examples of the displacement history in VIV cases. The segments used for analysis are different and denoted for each case.

at the node mode frequency, resulting in an amplitude of $\sim 0.05\,\overline{D}$. The overall VIV amplitude becomes significantly more pronounced at 30° AOA ($\sim 0.2\,\overline{D}$), and it continues to increase with AOA [Figs. 6(b) and 6(d)]. Several trends can be observed including the U_r^* corresponding to the peak VIV amplitude slightly increases with AOA; the U_r^* at which VIV starts to occur decreases with AOA; for AOA \geq 60°, the VIV persists even for high U_r^* , which is different from cases with a mass ratio of ~ 10 (Wei *et al.*, 2023) where the response diminishes

after the peak response. However, the peak amplitude at higher AOAs are comparable [Fig. 6(d)].

Different from the distinct amplitude branches observed for circular cylinders with low mass ratio and damping (Govardhan and Williamson, 2000), the change of the VIV amplitude of the USWs appears to be more gradual. However, the gradualness might not solely be attributed to the undulatory shape. Factors such as Reynolds number, mass ratio, and their combined effects could also play a role in

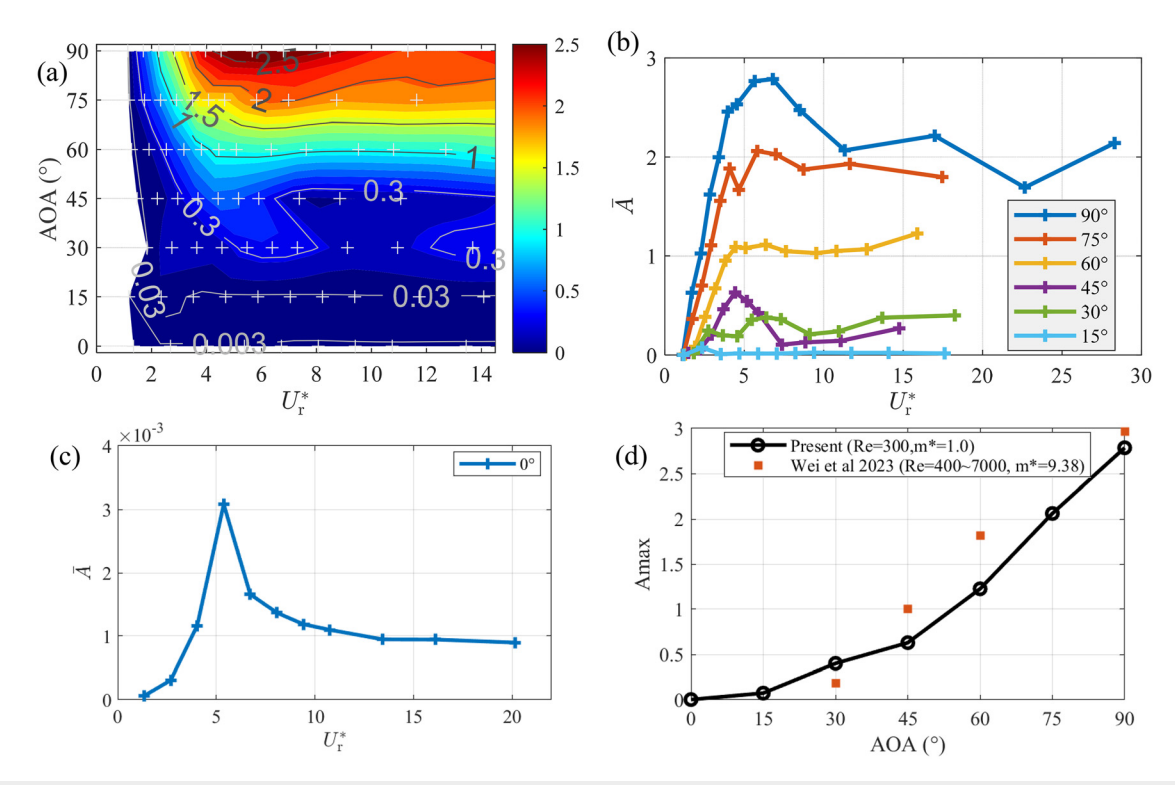


FIG. 6. (a) Contour plot of VIV amplitude, \overline{A} . (b) Line plots of VIV amplitude for AOAs $> 0^{\circ}$. (c) Line plot of VIV amplitude for AOA $= 0^{\circ}$. (d) Amax - AOA curve. Crosses in (a)–(c) indicate data points.

such changes, as reported in studies involving cylinders with various cross-sectional aspect ratios (Khalak and Williamson, 1996; Leontini *et al.*, 2006; Vijay *et al.*, 2020; and Willden and Graham, 2006). Identifying the underlying mechanism and parameters affecting this aspect of the VIV is beyond the scope of this study.

Force amplitude and phases

The total lift force, $F_{\rm L}$, is obtained by integrating the surface pressure and shear force from the flow. The amplitude of the lift force oscillation is computed in the same way as the displacement. To clearly demonstrate the trend of $F_{\rm L}$ oscillation amplitude with varying $U_{\rm r}$ across different AOAs, it is normalized by its maximum value at each given AOA and plotted in Fig. 7(a). Figure 7(b) plots the maximum amplitude of $F_{\rm L}$ oscillation at each AOA. From Fig. 7(a), one feature becomes immediately apparent: the lift force peaks just before the $U_{\rm r}^*$ where the vortex shedding frequency intersects with the in-water natural frequency, $f_{\rm nw}$ (as indicated by the dashed black line), especially for AOA 45° and above. This trend was previously reported in Govardhan and Williamson (2000) for VIV of low mass-damping circular cylinders.

Due to the added mass effect underwater, a significant component of the total lift force is the added-mass force, $F_{\rm am}$, computed as $F_{\rm am} = -c_{\rm am} m \ddot{y}$, where $c_{\rm am}$ is the added-mass coefficient (details of its calculation can be found in the Appendix) and y is the cross-flow displacement. When the added-mass force is subtracted from the total lift force, the remainder can be called the vortex force for convenience, i.e., $F_{\rm vor} = F_{\rm L} - F_{\rm am}$. While it is not exclusively due to vortex, the vortex force is intricately linked to vortex dynamics and to the convection of vorticity. Similar decomposition has been used in analysis of VIV circular cylinders (Govardhan and Williamson, 2000). Based on this decomposition, the VIV system can be formulated in two slightly different ways:

$$m\ddot{y} + c\dot{y} + ky = F_L,$$

or

$$(m + m_A)\ddot{y} + c\dot{y} + ky = F_{vor}.$$

Here, m, c, and k denote the mass, damping, and stiffness of the system, respectively. $m_A = c_{\rm am} m$ is the added mass. The two

formulations provide distinct perspectives on the VIV responses, offering a comprehensive understanding of the system dynamics. In the first formulation, resonance coincides with the lift force frequency aligning closely with the in vacuo natural frequency, while in the second formulation, resonance coincides with the vortex shedding frequency closely matching the in-water natural frequency. The phases of the vortex force and total lift force in relation to displacement, denoted by ϕ_{vor} and ϕ_{tot} , respectively, were computed for further analysis. These phases were calculated for dominant frequencies and are plotted separately in Figs. 8(a) and 8(b). Specifically, the phase angles were calculated from the complex frequency spectrum for displacement, vortex force, and lift. Since the data correspond to the same time period, the difference between the phase angles computed this way is the phase difference. In cases with multiple frequency components, the phases were calculated independently for each frequency component. However, only the phase of the frequency following the trend from stationary whisker vortex shedding is shown in the contour plots. For $AOA = 15^{\circ}$, the phases of the saddle mode frequency are shown.

In Fig. 8(a), the black dash-dot line with cross symbols indicates the U_r^* where the vortex shedding frequency intersects with the inwater natural frequency, while in Fig. 8(b), the black dash line with circle symbols indicates the $U_{\rm r}^*$ where the vortex shedding frequency intersects with the in vacuo natural frequency. Studies on the VIV of a circular cylinder revealed that the typical three-branch amplitude response is closely linked to the phases of these forces (Govardhan and Williamson, 2000). Although the three-branch amplitude response is not observed in the USWs, both the vortex force and total lift force phases exhibit 180° shifts. At AOA = 30° and below, the 180° vortex force phase jump occurs around the intersection of the vortex shedding frequency and the in-water natural frequency, while the 180° jump of the total lift force phase occurs around the intersection of the vortex shedding frequency and the in vacuo natural frequency. This suggests that in-water resonance causes the phase jump of the vortex force, while in vacuo resonance causes the phase jump of the total force. A similar behavior was observed in the response of elastically mounted circular cylinders with low mass ratios (Govardhan and Williamson, 2000). For AOA above 30°, both the vortex force phase and total lift force phase change gradually with $U_{\rm r}^*$ around in-water resonance and in vacuo resonance, respectively. At those high AOAs, the presence of multiple frequency components indicates a complex

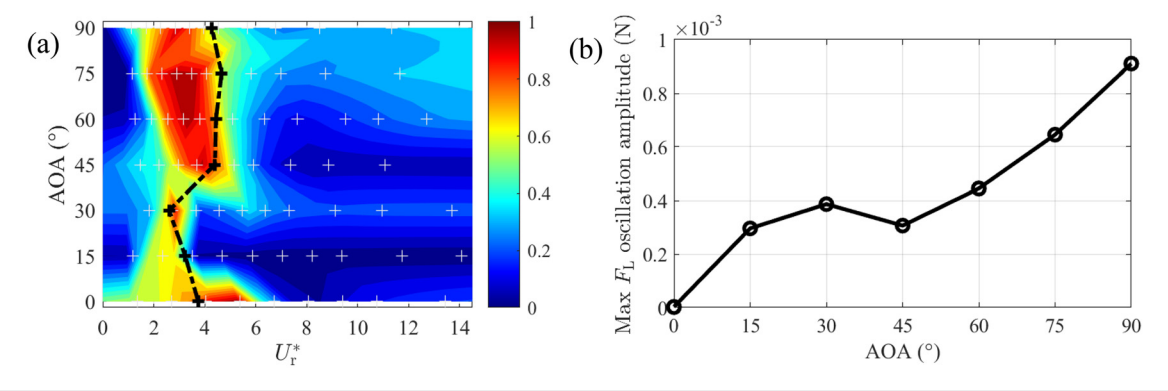


FIG. 7. (a) Contour plot of the lift force normalized by its maximum value at each given AOA. The dashed line indicates the U_r^* where the vortex shedding frequency intersects with the in-water natural frequency. (b) The maximum value of the lift force at each AOA.

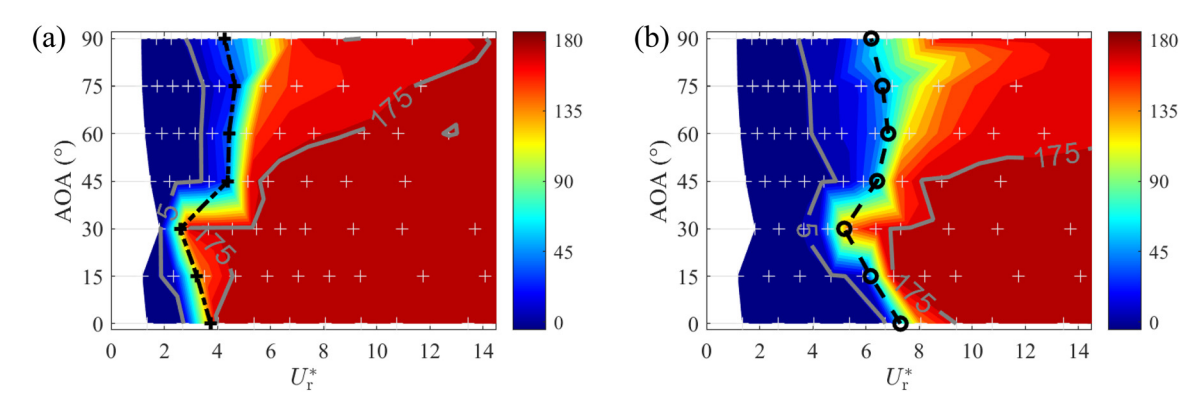


FIG. 8. (a) Contour plot of the vortex force phase in relation to the displacement. The black dash-dot line with cross symbols indicates the U_r^* where the vortex shedding frequency intersects with the in-water natural frequency. (b) Contour plot of the total lift force phase in relation to the displacement. The black dash line with circle symbols indicates the U_r^* , where the vortex shedding frequency intersects with the *in vacuo* natural frequency.

interplay between the structure and the wake flow. The nonlinear dynamics involved may lead to a transition from a sharp alternation to a more gradual modulation in force phases upon encountering resonance conditions.

Frequency response

The spectra of the displacement, lift force and vortex force at $AOA = 0^{\circ}$ are assembled in Fig. 9. The dominant VIV frequency for $AOA = 0^{\circ}$ remains a constant of \sim 0.19 across the range of $U_{\rm r}^*$, which is the vortex shedding frequency of the stationary whisker. It is mostly unaffected by either the in-water natural frequency or the *in vacuo* natural frequency. Only a small influence is seen at $U_{\rm r}^* = 2.7$, where a secondary component appears near $f_{\rm nw}$. The phase shifts in the vortex force and total lift force discussed in the section "Force amplitude and phases" appear not to change the frequency response. This is because the amplitude of oscillation is so small $(O(10^{-3}))$ that it has negligible effect on the wake dynamics. It should be noted that the incoming flow speed is a constant in the current study. If the swimming speed were to change, the frequency response at $AOA = 0^{\circ}$ would adhere to the Strouhal law, establishing a linear relationship between the frequency and swimming

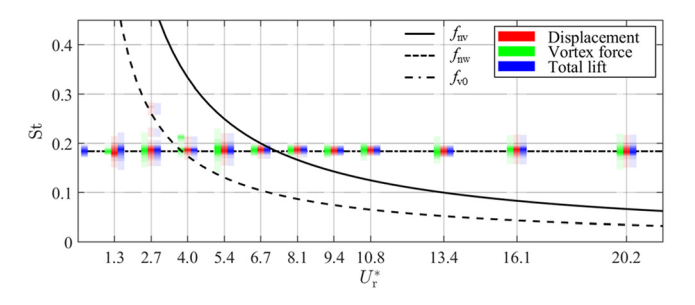


FIG. 9. Frequency spectra of the displacement, lift force and vortex force at $AOA = 0^{\circ}$. The spectrum is represented by color saturation where more saturated color stripes represent higher amplitude for the corresponding frequency component. Spectra of the three variables for the same reduced velocity are grouped and centered on the corresponding reduced velocity. The width of the stripes is chosen to be enough to show the spectra. f_{v0} is the vortex shedding frequency of the stationary whisker

speed. Miersch *et al.* (2011) also reported the existence of a dominant frequency in the VIV response at zero AOA for harbor seal whiskers, with this frequency positively scaling with swimming speed.

The frequency responses for AOAs $> 0^{\circ}$ cases are compiled in Fig. 10. The frequency is normalized by f_{nw} . It should be noted that in these figures, only dominant frequencies of VIV (highest spectral peak) are plotted against reduced velocity. While significant harmonics or noises are present in some cases, for clarity, the following discussions focuses solely on those dominant frequencies. Solid marker points indicate the dominant VIV frequency, while larger hollow square boxes indicate the dominant vortex force frequency, representing the vortex shedding dynamics. Several straight lines are also included to elucidate the frequency relationships: a solid horizontal line denotes f_{nw} , while a dash-dot horizontal line denotes the ratio of $f_{\rm nv}$ to $f_{\rm nw}$, which varies with AOA. Oblique lines depict constant Strouhal numbers derived from the vortex shedding frequencies in the stationary cases [see Fig. 4(b)]. In cases where multiple shedding frequencies are observed, such as AOA = 15° and AOA = 30°, multiple oblique lines are plotted accordingly.

From these plots, it is evident that VIV constantly initiates at the stationary vortex shedding frequency across all AOAs. This is indicated by the alignment of the displacement frequency and vortex force frequency, which coincide with the constant stationary Strouhal lines. As the reduced velocity U_r^* increases, the phenomenon of lock-in becomes observable across all cases, as indicated by both displacement frequency and vortex force frequency aligning with the in-water natural frequency. However, the characteristics of lock-in vary greatly with AOA.

At AOA = 15°, the dominant frequency response initially begins with the saddle mode (St* = 0.162). As U_r^* increases to around 2.3, a lock-in phenomenon between the node mode (St* = 0.217) and the inwater natural frequency occurs due to their close proximity. Subsequently, as U_r^* continues to increase, the dominant frequency responses revert back to the saddle mode, with another lock-in observed between the saddle mode and the in-water natural frequency at approximately U_r^* = 5.9. Notably, after these transitions, the dominant frequency of the vortex force consistently follows the saddle mode. Interestingly, at U_r^* where the dominant vortex force frequency surpasses the *in vacuo* natural frequency, the dominant frequency of

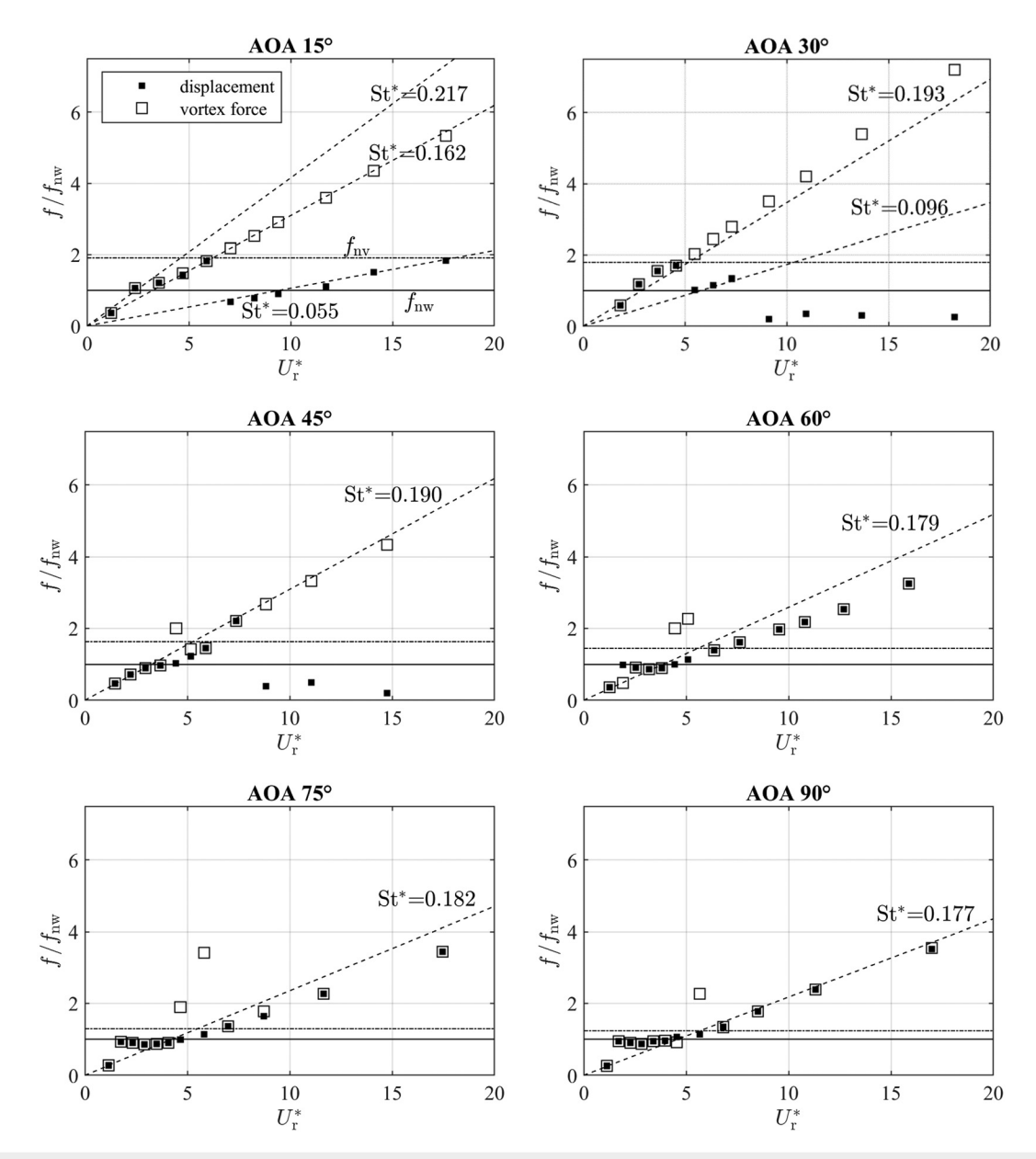


FIG. 10. Frequency response for AOA from 15° to 90°. Only the most dominant frequency component for each reduced velocity is included in the plots.

displacement abruptly shifts to the beating mode ($St^* = 0.055$), diverging from the response of vortex force. This divergence is likely attributed to the proximity of the beating mode to the in-water natural frequency.

At AOA = 30°, the dominant frequency response initially follows the stationary vortex shedding (St* = 0.193). Lock-in occurs between $U_r^* = 2.7$ and 4.6 with elevated frequencies. When the dominant frequency of the vortex force surpasses the *in vacuo* natural frequency at $U_r^* = 5.5$, while itself still adhering to St* = 0.193, the dominant frequency response of displacement abruptly shifts to its 1/2 subharmonic (St* = 0.096). This shift is likely attributable to the proximity of the

subharmonic to the in-water natural frequency. This transition to 1/2 subharmonic has also been observed for an elliptical cylinder of the same mass ratio (Leontini *et al.*, 2018). At $U_r^* = 9.1$, as the subharmonic frequency further deviates from the in-water natural frequency, a very low-frequency component emerges in the oscillation, becoming a prominent feature in the displacement frequency response.

For AOA \geq 45°, the dominant frequency response initially adheres to the static wake Strouhal number, and a more prominent lock-in phenomenon is observed across a wider range of $U_{\rm r}^*$. One particularly interesting observation in these cases is the behavior of the vortex force frequency. It suddenly jumps to a superharmonic of the

(a)

0.5

displacement frequency when the constant Strouhal line crosses the in-water natural frequency. Then, as the Strouhal line crosses the *in vacuo* natural frequency, it jumps back to the displacement frequency. The low dominant frequencies in displacement observed when AOA is below 30° only appear in AOA = 45° when U_r^* exceeds 8.8. However, significant low frequency components in displacement are observed for AOA ranging from 60° to 90°.

Similarly, a low frequency component with significant amplitude was observed in the experiment study by Wei *et al.* (2023), where it was more pronounced in the intermediate AOAs, particularly at 30° and 45°. In their study, the authors attributed this frequency to the beating vibration of the whisker model. However, in our study, unlike the beating frequency observed in the AOA = 15° cases, there appears to be no occurrence of two frequencies for the beat to occur. Here we use one case ($U_r^* = 10.9$ at AOA = 30°) to investigate the nature of the low frequency component of the VIV, since the low frequency oscillation was not only dominant but also contributed significantly to the large VIV amplitude [see Fig. 6(b)]. A spectrogram analysis [Fig. 11(a)] of the lift force history unveils further insights. The three

frequency bands are the low frequency (\sim 0.015), the vortex shedding frequency (\sim 0.2), and the harmonic of the vortex shedding frequency.

It is clear, especially from the superharmonic, that the vortex shedding frequency (\sim 0.2) is modulated. The frequency of this modulation is found to be the same as the low frequency. In Fig. 11(b), the displacement history and the vortex shedding frequency are aligned to illustrate the mechanism of the modulation. Specifically, when the whisker is at the extreme locations of the low frequency oscillation [e.g., t_1 and t_3 in Fig. 11(b)], the frequency is very close to the mean value [horizontal dashed line Fig. 11(b)]. This is because the whisker velocity is zero and the effective AOA remains unchanged. At the mid positions [e.g., t_2 and t_4 in Fig. 11(b)], the supposition of the whisker motion and the incoming flow changes the effective AOA and consequently the shedding frequency following the trend of the static vortex frequency with respect to AOA (see Fig. 4). There is a roughly 90° phase difference between the low frequency oscillation and the vortex shedding frequency.

The origin of this low frequency oscillation was initially suspected to be related to the computational domain length since the non-

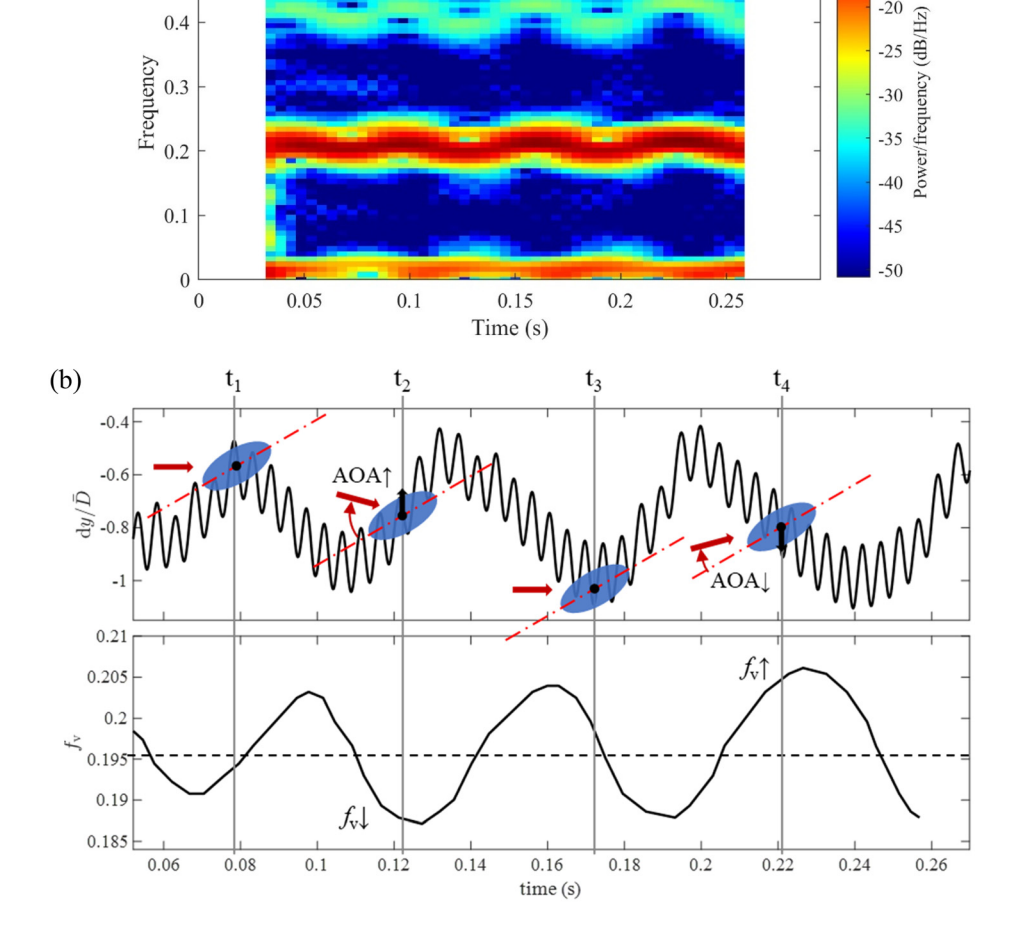


FIG. 11. (a) Spectrogram of the lift force for AOA = 30° , $U_r^* = 10.9$. (b) Schematic illustrating the mechanism of the modulation of the vortex shedding frequency. The red arrows indicate the vector sum of the velocity of the incoming flow and of the whisker (black arrows). In both plots, the frequency is nondimensional.

dimensional time it took for the inflow to travel through the domain was 60, which corresponded to a frequency of \sim 0.017. A cursory test was carried out for the $U_r^*=10.9~{\rm AOA}=30^\circ$ case, in which the domain length was extended by adding 256 uniform grid intervals beyond the original domain. The same phenomena persisted. Further analysis also reveals that this low frequency oscillation was not a transient phenomenon resulting from the initial condition either, because it could develop at later stages in the simulation and did not die out over time. In fact, in the demonstration case [Fig. 11(b)], it appeared to be getting stronger over time. An extremely low frequency, large-scale, and almost periodic component corresponding to an St of 0.0064 was elaborated in Lehmkuhl *et al.* (2013) for flow past a stationary circular cylinder. The low frequency arises from the periodic shrinkage and enlargement of the recirculation region. The low frequency oscillation here could be introduced through similar mechanisms.

Wake structure and DMD analysis

Model reduction techniques such as proper orthogonal decomposition (POD) and dynamic mode decomposition (DMD) have been used extensively in past studies (Chu *et al.*, 2021; Wang and Liu, 2016, 2017; and Witte *et al.*, 2012) to extract principal modes of flow field

around the USWs. Such decompositions have proven to be instrumental in understanding the complex vortex shedding patterns of the USWs, especially when the flow contains multiple frequency components. So far, it has been limited to analysis of flow past stationary seal whiskers. Here, we extend its usage to the flow around oscillating whiskers. Although DMD was carried out for all simulated cases, only results for several representative cases are reported here with the focus on understanding the VIV response of USWs.

Figure 12 shows the wake structure and dominant DMD modes at AOA = 0° for two specific reduced velocity values, one corresponding to the maximum amplitude at this AOA and the other being the largest $U_{\rm r}$ tested. As demonstrated in the wake structures [Fig. 12(a)], the hairpin vortex is undisturbed by the VIV throughout the range of reduced velocity. DMD decomposition of the flow field reveals highly organized dominant modes at the fundamental frequency and superharmonics [Fig. 12(b)], with the first two modes of $U_{\rm r}=2$ plotted in Fig. 12(c).

Figure 13 shows the wake structure and dominant DMD modes of the flow past a stationary USW at AOA = 15°. The wake structure [depicted in Fig. 13(a)] reveals a strong alternating shedding of a spanwise vortex tube, which becomes distorted at the saddle region. Secondary streamwise vortex tubes are also observed at the further

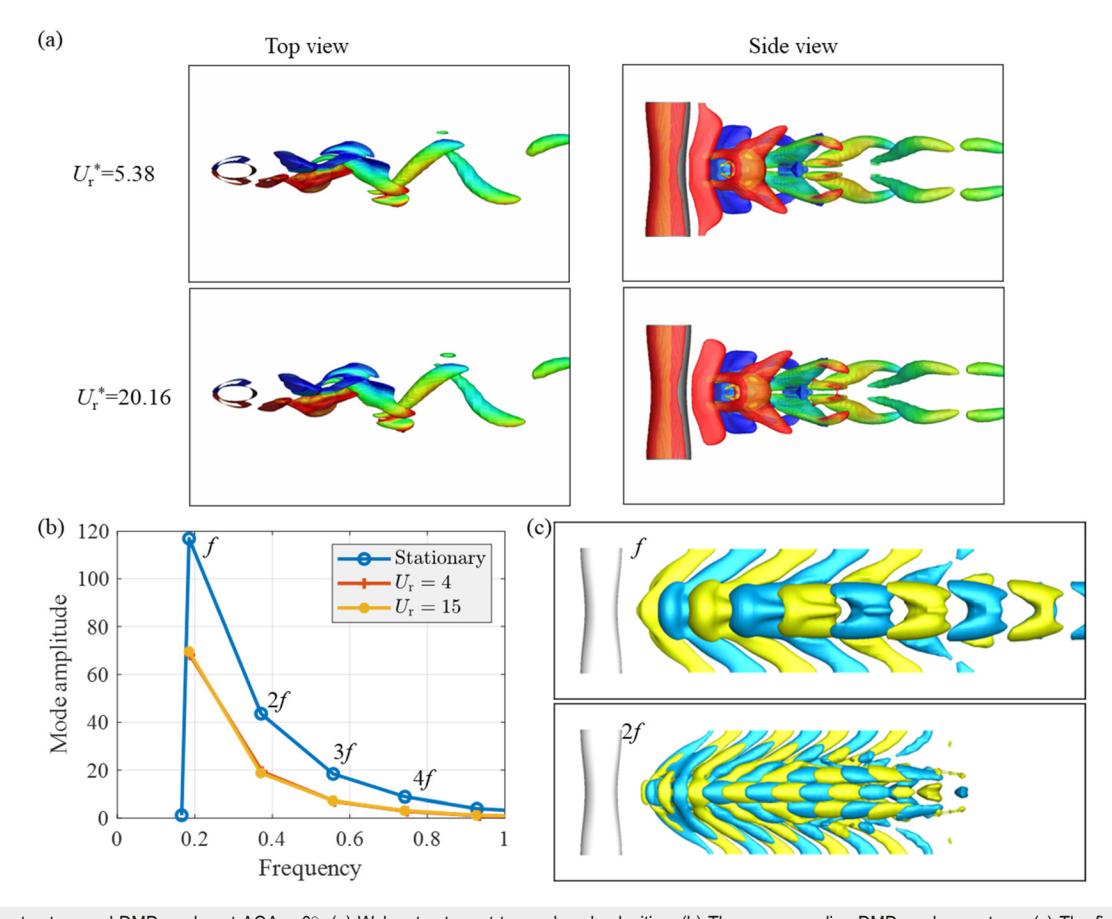


FIG. 12. Wake structure and DMD modes at AOA = 0° . (a) Wake structure at two reduced velocities. (b) The corresponding DMD mode spectrum. (c) The first two dominant modes visualized by the iso-surface of X velocity (streamwise).

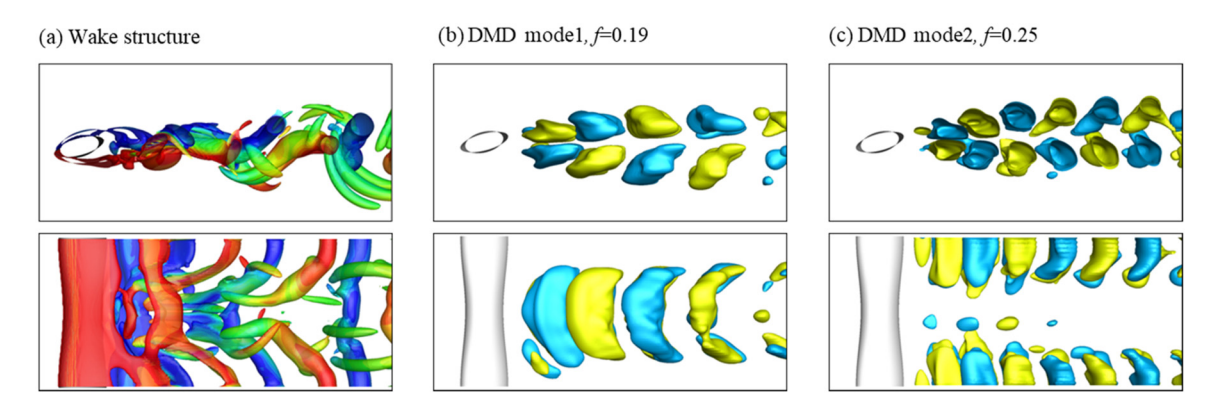


FIG. 13. Wake structure (a) and the dominant DMD modes (b) and (c) of the flow past stationary USW at AOA = 15°. The top row is from the top view. The bottom row is from the side view.

downstream of saddle region. Figure 13(b) illustrates the two DMD modes corresponding to the two dominant frequencies observed in the lift force spectrum. Both modes exhibit alternating patterns, indicating the alternating shedding of spanwise vortices. Two modes are confined to two different spanwise regions: saddle region and node region. The saddle mode has a frequency close to that of the hairpin vortex (f=0.19), while the node mode has a higher frequency (f=0.25).

Figure 14 shows the change of DMD modes with three different reduced velocity for AOA = 15° , which is best illustrated from the side view. $U_{\rm r} = 2$ is the case where resonant oscillation occurs due to proximity of the in-water natural frequency and the node plane vortex mode. In this case, the node mode is strengthened, as evidenced by the extension of vortex tube into the saddle plane. Conversely, the

coherence of saddle mode is disrupted, despite the persistence of the saddle mode frequency. As the reduced velocity increases, the modes gradually revert to the stationary pattern. Notably, the $U_{\rm r}\!=\!10$ case exhibits essentially identical dominant DMD modes as the stationary case.

Figure 15 shows the wake structure and the dominant DMD modes for the case AOA = 30, $U_r^* = 10.9$. The previously discussed low frequency mode was also successfully captured by the DMD analysis. Figure 15(c) illustrates the mode structure, which is characterized by very long, streamwise stretched wake structures spanning the whole domain. The same type of low frequency DMD mode was consistently observed across various AOA and U_r cases. Interestingly, a similar low-frequency mode was reported in Govardhan and Williamson

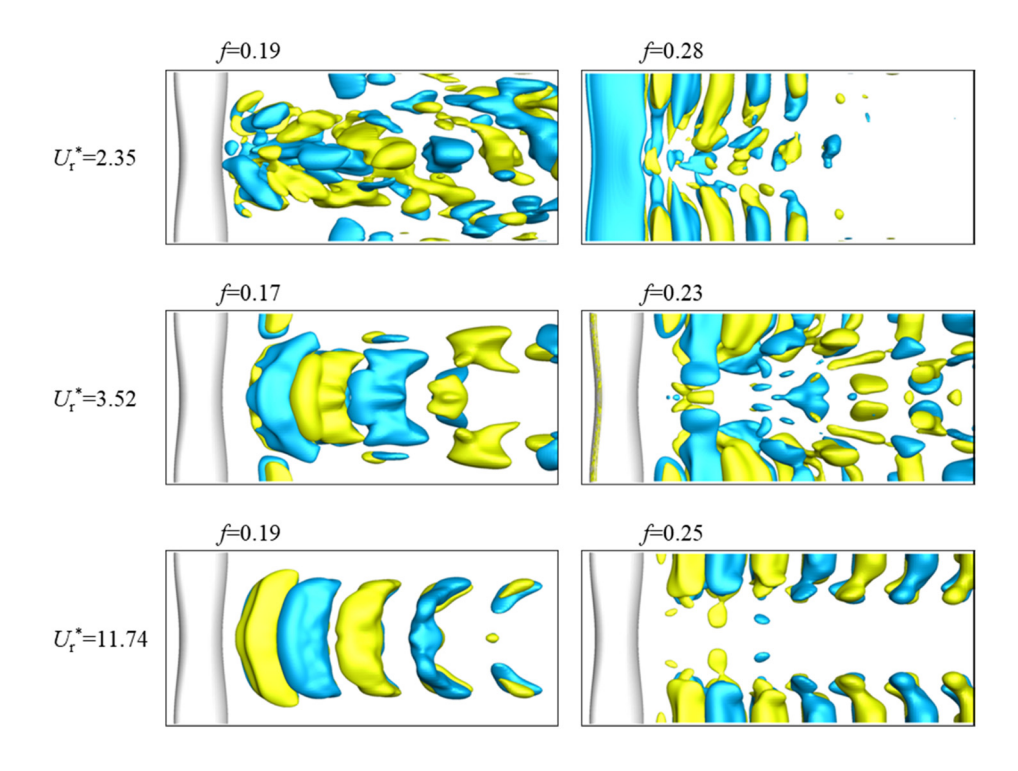


FIG. 14. Change of dominant DMD mode with reduced velocity for $AOA = 15^{\circ}$. All subfigures are from side view.

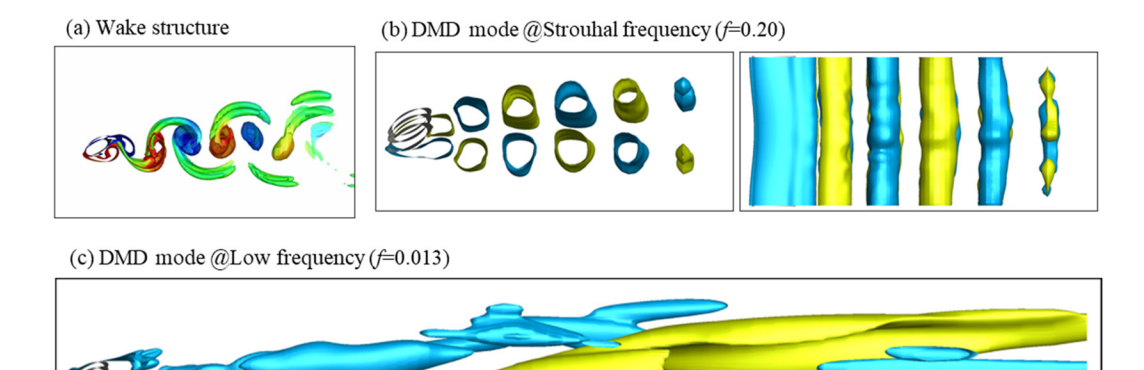


FIG. 15. Wake structure [(a) top view] and the dominant DMD modes [(b) top view and side view; and (c) top view] for AOA = 30° , $U_r^* = 10.9$.

(2005) for VIV of a sphere, which "represents a low-oscillation frequency relative to the frequency of vortex formation for the static sphere."

Representative DMD modes at high AOAs are plotted in Fig. 16. Generally, the most dominant DMD mode corresponds to the Kámán vortex shedding of the wake. For small U_r^* , both the wake and the DMD mode appear similar to the stationary counterparts. The VIV tends to strengthen the spanwise coherence of the Kámán vortices, as seen in AOA = 60° , $U_r^* = 1.27$ and AOA = 90° , $U_r^* = 2.27$. As the VIV amplitude increases, the vortices shed at each half cycle become more separated. Correspondingly, the DMD mode

shows two streaks of alternating iso-velocity pairs. This is most evident in AOA = $90^\circ,\,U_r^*=2.27.$ As the U_r^* further increases (close to and beyond the maximum VIV amplitude), the spanwise vortices become less coherent. This can be seen from the lack of continuous spanwise structure in the dominant DMD modes in cases AOA = $60^\circ,\,U_r^*=5.08$ and AOA = $90^\circ,\,U_r^*=8.49.$ It would be interesting if the DMD modes could reveal the subtle differences between the vortex shedding patterns associated with the jumps of the dominant vortex shedding frequency shown in Fig. 10. However, the attempt at this was not fruitful and is therefore not included here.

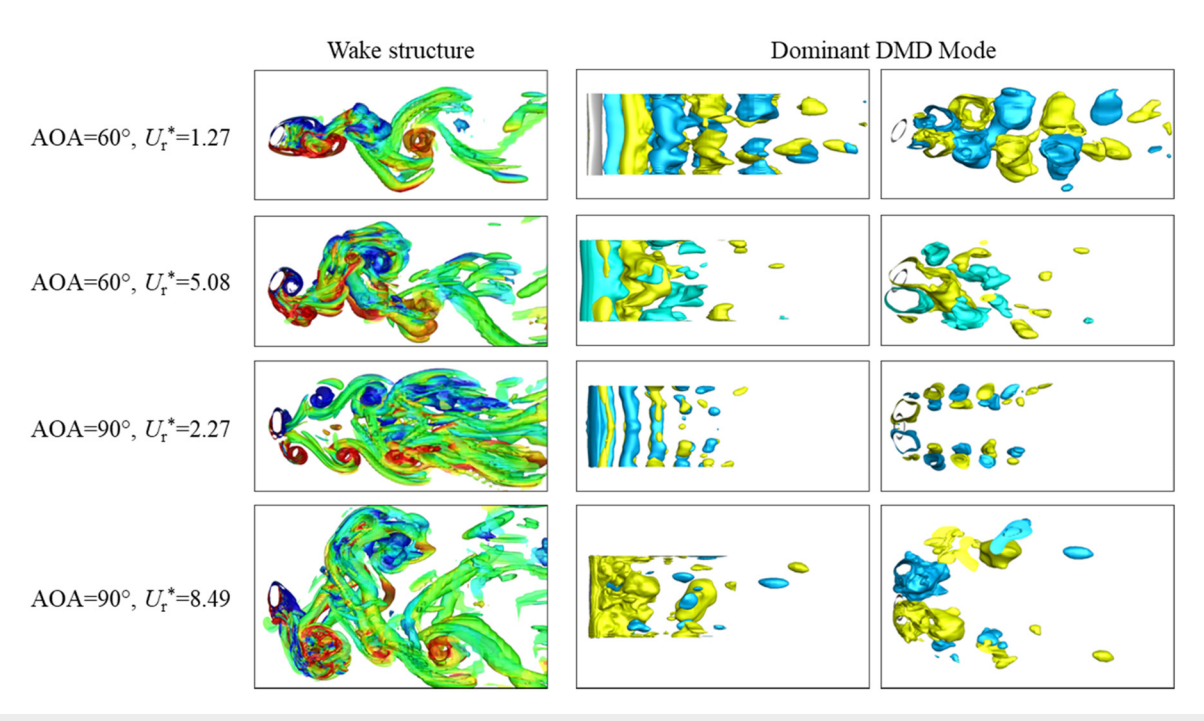


FIG. 16. Wake structure and dominant DMD mode of some high AOA cases. For AOA = 60° , $U_{\rm f}^* = 5.08$, the iso-value is slightly smaller than the rest to reveal the structure.

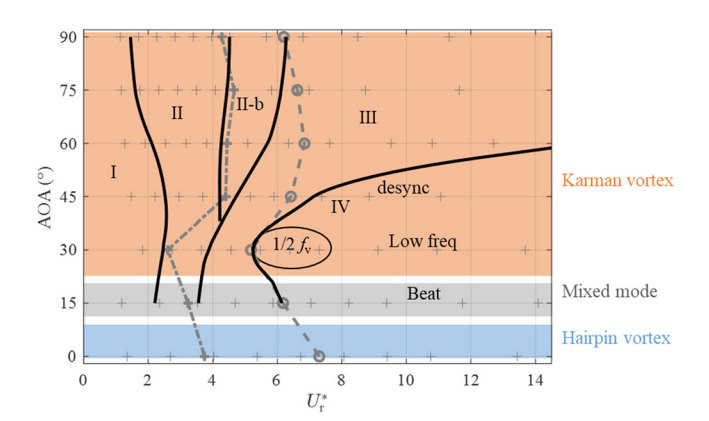


FIG. 17. VIV response regimes of the USW. The two dashed gray lines are from Fig. 8, indicating the $U_{\rm r}^*$ where the vortex shedding frequency crosses $f_{\rm nw}$ and $f_{\rm nv}$, respectively.

Regimes of response

Given the analysis of various aspects of VIV response, we have undertaken the task of partitioning the space into distinct response regimes. While it could be conceivable to categorize these regimes based on wake patterns—specifically, the number of vortices shed during each cycle, as commonly practiced in VIV systems—we opted against this approach for several reasons: the wake structure exhibits complexity, including spanwise variation, making it challenging to precisely determine the number of vortices, particularly for cases beyond the rising side of the amplitude curves. Conventional labels commonly used to describe vortex patterns may not suffice to capture the intricacies observed in our analysis. Instead, the division of regions primarily relies on the frequency response observed in our analysis.

Based on the flow characteristics of the stationary cases, the entire space can be divided into three regions based on AOAs: the hairpin vortex region, the mixed vortex region, and the Karman vortex region. This reflects the change of driving force with AOA. The approximate boundaries of the three regions lie between 0° and 15°, and 15° and 30°, respectively. In the hairpin vortex region, the vortex dynamics remain essentially unaffected by the oscillation. For the other two regions, the vortex dynamics change with reduced velocity, and this change also depends on AOA. Consequently, we further partitioned

the mixed vortex and Karman vortex regions into five subregions, as illustrated in Fig. 17.

In region I, the oscillation follows the vortex shedding frequency, and while the amplitude increases with reduced velocity, it is not significant enough to alter the vortex dynamics.

Region II is characterized by both vortex shedding and oscillation locking to the in-water natural frequency. The response amplitude gradually increases and the vortex shedding pattern is similar to the 2S mode (two single vortex in one oscillation cycle) commonly observed in VIV of circular cylinders.

In region II-b, the vortex force exhibits dominant superharmonics while the dominant oscillation frequency corresponds to in-water natural frequency of the system. This region bears some similarity to the high branch of low mass-damping circular cylinders where the vortex phase has a 180° to the displacement. The appearance of superharmonics suggests vortex modes similar to the 2P mode (two pairs of vortices in one oscillation cycle contributing to the superharmonic in the vortex force spectrum). The appearance of region II-b might be related to change in added mass with AOA. The driving vortex force increases with AOA, while the total mass (material and added) decreases with AOA. Indeed, the transition from the I-II-III response type to the I-II-IIb-III response type resembles the two branch and three branch response types as the mass ratio decreases. The increase in effective Re with AOA could contribute to the occurrence of the II-b region as well. Govardhan and Williamson (2006) showed that for Re < 500, only two branches exist even for low mass ratio circular cylinders.

In region III, both the oscillation and vortex shedding align with the stationary vortex shedding frequency. For AOA 15° – 45° , oscillation amplitude decreases in this region. For AOA> = 60, the oscillation amplitude remains high in this region, which is also commonly observed in both circular and elliptical cylinders with mass ratio lower than the critical value, termed infinite lock-in regime.

Region IV is characterized by the vortex shedding frequency following a constant Strouhal number while low frequency oscillation dominates. For AOA> = 60° , while low frequency oscillation component is also present, the dominant oscillation frequency is the vortex shedding frequency. Thus, region IV does not appear. For AOA 15° – 45° , there are several special subregions in this regime. At 15° , the low frequency is the beat frequency of the two vortex shedding frequencies. At AOA = 30° , oscillation first locks to the 1/2 subharmonic of the vortex shedding, then is modulated by a low frequency. At 45° , the oscillation desynchronizes, leading to a very low amplitude. However,

TABLE II. Summary of grid study.

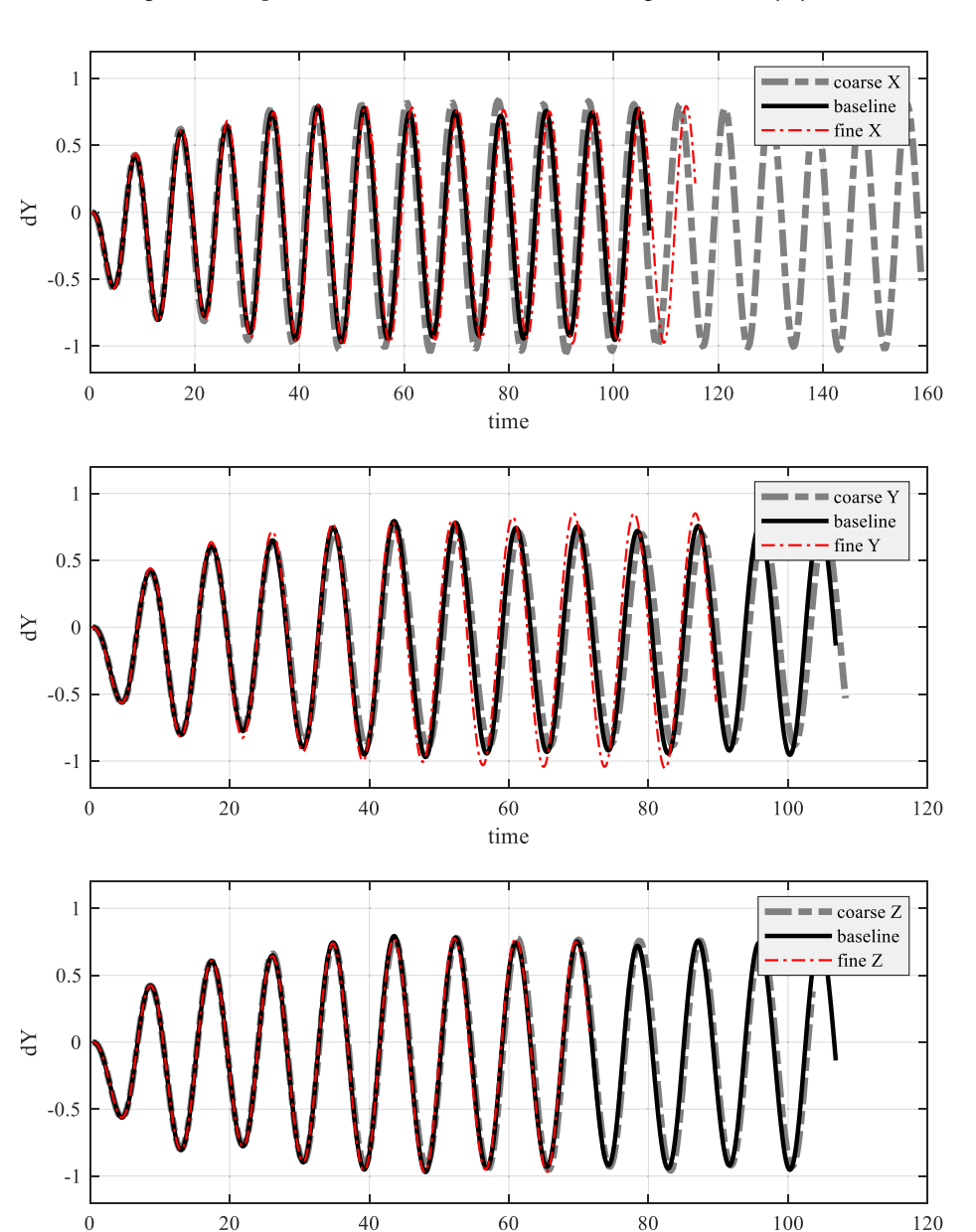
Label	Number of grid points			Minimum grid interval			VIV results			
	X	Y	Z	X	Y	Z	Amplitude	Error%	Frequency	Error%
Baseline	257	257	97	0.025	0.025	0.0625	1.676	0.0	0.1148	0.0
Coarse X	129	257	97	0.05	0.025	0.0625	1.858	9.8	0.1152	0.3
Fine X	513	257	97	0.015	0.025	0.0625	1.726	2.9	0.1145	-0.3
coarse Y	257	257	97	0.025	0.035	0.0625	1.584	-5.8	0.1142	-0.5
Fine Y	257	513	97	0.025	0.015	0.0625	1.872	10.5	0.1150	0.2
Coarse Z	257	257	65	0.025	0.025	0.0938	1.705	1.7	0.1145	-0.3
Fine Z	257	257	129	0.025	0.025	0.0469	1.710	2.0	0.1148	0.0

the boundaries between these subregions cannot be determined from current simulations.

CONCLUSION

The VIV of the USW was investigated in the full range of AOA and a wide range of reduced velocity at a low Reynolds number of 300. The vortex shedding of the whisker undergoes a transition from hairpin vortex mode at zero AOA to the classic Kármán vortex mode as the AOA increases. Through dynamic mode decomposition, a mixture of the two mode was found at the AOA of 15°. Along with this transition, the amplitude of the VIV increased by three orders of magnitude to up to three diameters at 90° AOA. At high

AOAs, the VIV response of the whisker shows many characteristics typical of circular and elliptical cylinders of a mass ratio close to 1, such as frequency lock-in and infinite lock-in branch. The results corroborate previous findings that the VIV suppression by the undulatory whisker morphology is only effective around zero AOA. This suggests that the seals adopt a zero angle of attack as the working condition and deviation from this condition caused by the external flow may be interpreted by its sensory system as signals. In addition to amplitude reduction of the lift force oscillation, the undulatory seal geometry also significantly reduces its frequency, which could be an optimization in regard to the frequency sensitivity of the seal's sensory system.



time

FIG. 18. Displacement history of case AOA = 60° , $U_r = 8$ using different girds.

One limitation of the current study is that the Reynolds number is fixed at 300. The effect of Reynolds number on the hairpin vortex shedding merits further investigation to cover the full range of seal swimming speed.

ACKNOWLEDGMENTS

This work was supported by NSF under Grant No. 2327204. The computation was supported by XSEDE (now ACCESS) under Award Nos. CTS180004 and MCH220042.

AUTHOR DECLARATIONS Conflict of Interest

The authors have no conflicts to disclose.

Author Contributions

Biao Geng: Conceptualization (equal); Data curation (lead); Formal analysis (equal); Investigation (equal); Methodology (equal); Writing – original draft (equal); Writing – review & editing (equal). Xudong Zheng: Conceptualization (equal); Formal analysis (equal); Investigation (equal); Methodology (equal); Project administration (equal); Writing – original draft (equal); Writing – review & editing (equal). Qian Xue: Conceptualization (equal); Formal analysis (equal); Funding acquisition (lead); Investigation (equal); Methodology (equal); Project administration (lead); Resources (equal); Supervision (lead); Writing – original draft (equal); Writing – review & editing (equal).

DATA AVAILABILITY

The data that support the findings of this study are available from the corresponding author upon reasonable request.

APPENDIX: TECHNICAL INFORMATION

Grid study

Previous static flow past whisker simulations using the same flow solver showed that a resolution of 0.025 D was adequate to resolve the geometric features of the whisker (Liu et al., 2019b). Further grid study were carried out to test the effect of VIV. The grid study was carried out using a test case (AOA = 60° and $U_{\rm r} = 8$), which had a large VIV amplitude in preliminary simulations. Due to the parallel algorithm of the flow solver, the number of grid intervals must be an integer power of 2, which limits the flexibility in grid refinement. The effect of grid resolution on the VIV was tested for each direction separately using a coarse and a fine grid. The configuration and results are summarized in Table II. Change of grid with respect to the baseline case are bolded. Figure 18 compares the VIV displacement history of the grid study cases. Generally, the baseline case has small errors in VIV amplitude and frequency compared to the fine grids except for the amplitude of the fine Y case where the error is 10.5%. However, the fine Y grid was not used to reduce the computational cost to make the parametric simulation feasible. For cases with large VIV amplitude, the grid number in the transverse direction is doubled to increase the size of the high resolution region to cover the range of VIV.

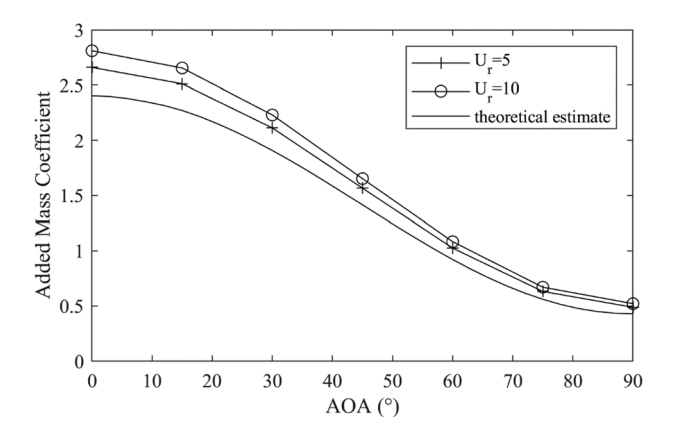


FIG. 19. Estimation of added mass coefficient for the whisker at different AOAs. Theoretical estimate is calculated as $c_{\rm am}=\int_0^\lambda \rho_{\rm water} \frac{\pi}{4} L_x^2 {\rm d}z/m_{\rm whisker}$, where L_x is the dimension of the whisker along the stream direction and $m_{\rm whisker}$ is the mass of the whisker

Added mass

Some numerical experiments were carried out to calculate in water natural frequency and the added mass of the whisker at different AOAs. For these experiments, the same setup described above was used. The difference was that no incoming flow was prescribed at the inlet. Instead, the whisker was first displaced from equilibrium position by a small displacement $(0.2 \overline{D})$. It was then released to undergo damped free vibration. With the displacement history in these experiments, it was possible to calculate the natural frequency and thus the added mass coefficient (c_{am}). The results are plotted in Fig. 19. Theoretical estimates using added mass for elliptical cylinders in planar potential flow (Limacher, 2021) are also included for comparison. There was a weak dependence on the stiffness of the spring. The actual added mass coefficient for the VIV cases are expected to slightly deviate from these values due to the incoming flow and change of oscillation amplitude. Nevertheless, they should give good enough estimates of the in water natural frequency during VIV.

With the estimated added mass coefficient for each AOA, the in water natural frequency was calculated as $f_{\rm nw} = \sqrt{\frac{K}{(1+c_{\rm am})M}}$, given that the density ratio is 1.

Dynamic mode decomposition

DMD was used to extract the spatial flow modes corresponding to each frequency component. For this purpose, the algorithm proposed by Schmid (2010) and implemented in the open source DMD package PyDMD (Demo *et al.*, 2018) was used. The flow field was sampled at about 50 snapshots per oscillation cycle for two to three cycles. The velocity field is arranged as a time sequence of column vectors that is input to the DMD algorithm. The real part of the DMD mode are used for visualization.

REFERENCES

Beem, H. R., Passive Wake Detection Using Seal Whisker-Inspired Sensing. Passive Wake Detection Using Seal Whisker-Inspired Sensing (MIT, 2015).

- Chu, S., Xia, C., Wang, H., Fan, Y., and Yang, Z., "Three-dimensional spectral proper orthogonal decomposition analyses of the turbulent flow around a seal-vibrissa-shaped cylinder," Phys. Fluids 33, 025106 (2021).
- Dehnhardt, G., Hyvärinen, H., Palviainen, A., and Klauer, G., "Structure and innervation of the vibrissal follicle-sinus complex in the Australian water rat, *Hydromys chrysogaster*," J. Comp. Neurol. **411**, 550–562 (1999).
- Dehnhardt, G., Mauck, B., and Bleckmann, H., "Seal whiskers detect water movements," Nature 394, 235–236 (1998).
- Dehnhardt, G., Mauck, B., Hanke, W., and Bleckmann, H., "Hydrodynamic trailfollowing in harbor seals (*Phoca vitulina*)," Science **293**, 102–104 (2001).
- Dehnhardt, G., Mauck, B., Thewissen, J. G. M., and Nummela, S., "Mechanoreception in secondarily aquatic vertebrates," in *Sensory Evolution on the Threshold: Adaptations in Secondarily Aquatic Vertebrates* (University of California Press Berkeley, 2008), pp. 295–314.
- Demo, N., Tezzele, M., and Rozza, G., "PyDMD: Python dynamic mode decomposition," J. Open Source Software 3, 530 (2018).
- Dunt, T. K., Heck, K. S., Lyons, K., Murphy, C. T., Cal, R. B., and Franck, J. A., "Wavelength-induced shedding frequency modulation of seal whisker inspired cylinders," Bioinspiration Biomimetics 19, 036004 (2024).
- Ferčák, O., Lyons, K. M., Murphy, C. T., Kamensky, K. M., Cal, R. B., and Franck, J. A., "Multicolor dye-based flow structure visualization for seal-whisker geometry characterized by computer vision," Bioinspiration Biomimetics 19, 016004 (2023).
- Gaster, M., "Vortex shedding from slender cones at low Reynolds numbers," J. Fluid Mech. 38, 565–576 (1969).
- Ginter, C. C., DeWitt, T. J., Fish, F. E., and Marshall, C. D., "Fused traditional and geometric morphometrics demonstrate pinniped whisker diversity," PLoS One 7, e34481 (2012).
- Gläser, N., Wieskotten, S., Otter, C., Dehnhardt, G., and Hanke, W., "Hydrodynamic trail following in a California sea lion (*Zalophus california-nus*)," J. Comp. Physiol., A **197**, 141–151 (2011).
- Govardhan, R. and Williamson, C. H. K., "Resonance forever: Existence of a critical mass and an infinite regime of resonance in vortex-induced vibration," J. Fluid Mech. 473, 147–166 (2002).
- Govardhan, R. and Williamson, C. H. K., "Modes of vortex formation and frequency response of a freely vibrating cylinder," J. Fluid Mech. **420**, 85–130 (2000)
- Govardhan, R. N. and Williamson, C. H. K., "Defining the 'modified Griffin plot' in vortex-induced vibration: Revealing the effect of Reynolds number using controlled damping," J. Fluid Mech. 561, 147–180 (2006).
- Govardhan, R. N. and Williamson, C. H. K., "Vortex-induced vibrations of a sphere," J. Fluid Mech. 531, 11–47 (2005).
- Graff, M. M., "Mechanisms of whisker based flow sensing," Ph.D. thesis (Northwestern University, 2016).
- Grant, R. A. and Goss, V. G. A., "What can whiskers tell us about mammalian evolution, behaviour, and ecology?," Mamm. Rev. **52**, 148–163 (2022).
- Hanke, W., Witte, M., Miersch, L., Brede, M., Oeffnet, J., Michael, M., Hanke, F., Leder, A., and Dehnhardt, G., "Harbor seal vibrissa morphology suppresses vortex-induced vibrations," J. Exp. Biol. 213, 2665–2672 (2010).
- Hans, H., Miao, J., Weymouth, G., and Triantafyllou, M., "Whisker-like geometries and their force reduction properties," in paper presented at the MTS/IEEE OCEANS—Bergen, 2013.
- Hans, H., Miao, J. M., and Triantafyllou, M. S., "Mechanical characteristics of harbor seal (*Phoca vitulina*) vibrissae under different circumstances and their implications on its sensing methodology," Bioinspiration Biomimetics 9, 036013 (2014).
- Hyvärinen, H. and Katajisto, H., "Functional structure of the vibrissae of the ringed seal (Phoca hispida Schr.)," Acta Zool. Fenn. 171, 17–30 (1984).
- Jie, H. and Liu, Y. Z., "Large eddy simulation and proper orthogonality decomposition of turbulent flow around a vibrissa-shaped cylinder," Int. J. Heat Fluid Flow 67, 261–277 (2017).
- Kamat, A. M., Zheng, X., Bos, J., Cao, M., Triantafyllou, M. S., and Kottapalli, A. G. P., "Undulating seal whiskers evolved optimal wavelength-to-diameter ratio for efficient reduction in vortex-induced vibrations," Adv. Sci. 11, 2304304 (2023).
- Khalak, A. and Williamson, C. H. K., "Dynamics of a hydroelastic cylinder with very low mass and damping," J. Fluids Struct. 10, 455–472 (1996).

- Kim, H. J. and Yoon, H. S., "Effect of the orientation of the harbor seal vibrissa based biomimetic cylinder on hydrodynamic forces and vortex induced frequency," AIP Adv. 7, 105015 (2017).
- Kurtulmuş, N., "Experimental investigation of flow structure and heat transfer characteristics for confined cylinders," Int. Commun. Heat Mass Transfer 133, 105959 (2022).
- Lehmkuhl, O., Rodríguez, I., Borrell, R., and Oliva, A., "Low-frequency unsteadiness in the vortex formation region of a circular cylinder," Phys. Fluids 25, 085109 (2013)
- Leontini, J. S., Griffith, M. D., Lo Jacono, D., and Sheridan, J., "The flow-induced vibration of an elliptical cross-section at varying angles of attack," J. Fluids Struct. 78, 356–373 (2018).
- Leontini, J. S., Thompson, M. C., and Hourigan, K., "The beginning of branching behaviour of vortex-induced vibration during two-dimensional flow," J. Fluids Struct. 22, 857–864 (2006).
- Limacher, E. J., "Added-mass force on elliptic airfoils," J. Fluid Mech. 926, R2 (2021).
- Liu, G., Geng, B., Zheng, X., Xue, Q., Dong, H., and Lauder, G. V., "An image-guided computational approach to inversely determine in vivo material properties and model flow-structure interactions of fish fins," J. Comput. Phys. 392, 578–593 (2019a).
- Liu, G., Xue, Q., and Zheng, X., "Phase-difference on seal whisker surface induces hairpin vortices in the wake to suppress force oscillation," Bioinspiration Biomimetics 14, 066001 (2019b).
- Lyons, K., Murphy, C. T., and Franck, J. A., "Flow over seal whiskers: Importance of geometric features for force and frequency response," PLoS One 15, e0241142–25 (2020).
- Marshall, C. D., Amin, H., Kovacs, K. M., and Lydersen, C., "Microstructure and innervation of the mystacial vibrissal follicle-sinus complex in bearded seals, *Erignathus barbatus* (Pinnipedia: Phocidae)," Anat. Rec. 288, 13–25 (2006).
- Miersch, L., Hanke, W., Wieskotten, S., Hanke, F. D., Oeffner, J., Leder, A., Brede, M., Witte, M., and Dehnhardt, G., "Flow sensing by pinniped whiskers," Philos. Trans. R Soc., B 366, 3077–3084 (2011).
- Mittal, R. and Balachandar, S., "Generation of streamwise vortical structures in bluff body wakes," Phys. Rev. Lett. 75, 1300–1303 (1995).
- Murphy, C. T., Eberhardt, W. C., Calhoun, B. H., Mann, K. A., and Mann, D. A., "Effect of angle on flow-induced vibrations of pinniped vibrissae," PLoS One 8, e69872 (2013).
- Murphy, C. T., Reichmuth, C., Eberhardt, W. C., Calhoun, B. H., and Mann, D. A., "Seal whiskers vibrate over broad frequencies during hydrodynamic tracking," Sci. Rep. 7, 8350 (2017).
- Murphy, C. T., Reichmuth, C., and Mann, D., "Vibrissal sensitivity in a harbor seal (*Phoca vitulina*)," J. Exp. Biol. **218**, 2463–2471 (2015).
- Papangelou, A., "Vortex shedding from slender cones at low Reynolds numbers," J. Fluid Mech. **242**, 299–321 (1992).
- Radi, A., Thompson, M. C., Sheridan, J., and Hourigan, K., "From the circular cylinder to the flat plate wake: The variation of Strouhal number with Reynolds number for elliptical cylinders," Phys. Fluids 25, 101706 (2013).
- Rinehart, A., Shyam, V., and Zhang, W., "Characterization of seal whisker morphology: Implications for whisker-inspired flow control applications," Bioinspiration Biomimetics 12, 066005 (2017).
- Schmid, P. J., "Dynamic mode decomposition of numerical and experimental data," J. Fluid Mech. 656, 5–28 (2010).
- Shatz, L. F. and de Groot, T., "The frequency response of the vibrissae of harp seal, *Pagophilus groenlandicus*, to sound in air and water," PLoS One 8, e54876
- Sofroniew, N. J. and Svoboda, K., "Whisking," Curr. Biol. 25, R137–R140 (2015).
 Song, L., Ji, C., Yuan, D., Xu, D., Zhang, X., Wei, Y., and Yin, T., "Single degree-of-freedom flow-induced vibration of an elastically-supported harbor seal whisker model: An experimental study," Lixue Xuebao/Chin. J. Theor. Appl. Mech. 54, 653–668 (2022).
- Tombazis, N. and Bearman, P. W., "A study of three-dimensional aspects of vortex shedding from a bluff body with a mild geometric disturbance," J. Fluid Mech. 330, 85–112 (1997).
- Vijay, K., Srinil, N., Zhu, H., Bao, Y., Zhou, D., and Han, Z., "Flow-induced transverse vibration of an elliptical cylinder with different aspect ratios," Ocean Eng. 214, 107831 (2020).

- Wang, S. and Liu, Y., "Wake dynamics behind a seal-vibrissa-shaped cylinder: A comparative study by time-resolved particle velocimetry measurements," Exp. Fluids 57, 32 (2016).
- Wang, S. and Liu, Y. Z., "Flow structures behind a vibrissa-shaped cylinder at different angles of attack: Complication on vortex-induced vibration," Int. J. Heat Fluid Flow 68, 31–52 (2017).
- Wei, Y., Ji, C., Yuan, D., Song, L., and Xu, D., "Experimental study on the effect of the angle of attack on the flow-induced vibration of a harbor seal's whisker," Fluids 8, 206 (2023).
- Willden, R. H. J. and Graham, J. M. R., "Three distinct response regimes for the transverse vortex-induced vibrations of circular cylinders at low Reynolds numbers," J. Fluids Struct. 22, 885–895 (2006).
- Williamson, C. H. K. and Govardhan, R., "Vortex-induced vibrations," Annu. Rev. Fluid Mech. 36, 413–455 (2004).
- Witte, M., Hanke, W., Wieskotten, S., Miersch, L., Brede, M., Dehnhardt, G., and Leder, A., "On the wake flow dynamics behind harbor seal vibrissae—A fluid mechanical explanation for an extraordinary capability," in *Nature-Inspired Fluid Mechanics: Results of the DFG Priority Programme 1207 "Nature-Inspired Fluid Mechanics" 2006–2012*, Notes on Numerical Fluid Mechanics and Multidisciplinary Design, edited by C. Tropea and H. Bleckmann (Springer, Berlin, Heidelberg, 2012), pp. 271–289.
- Zheng, X., Kamat, A. M., Cao, M., and Kottapalli, A. G. P., "Creating underwater vision through wavy whiskers: A review of the flow-sensing mechanisms and biomimetic potential of seal whiskers," J. R Soc. Interface 18, 20210629 (2021).